

# A SCALABLE PARALLEL FINITE ELEMENT FRAMEWORK FOR GROWING GEOMETRIES. APPLICATION TO METAL ADDITIVE MANUFACTURING.

ERIC NEIVA, SANTIAGO BADIA, ALBERTO F. MARTÍN, AND MICHELE CHIUMENTI

Universitat Politècnica de Catalunya (UPC), Jordi Girona 1-3, Edifici C1, 08034 Barcelona, Spain.

Centre Internacional de Mètodes Numèrics en Enginyeria (CIMNE), Building C1,  
Campus Nord UPC, Gran Capitán S/N, 08034 Barcelona, Spain.

{eneiva, sbadia, amartin, michele}@cimne.upc.edu.

**ABSTRACT.** *This work introduces an innovative parallel, fully-distributed finite element framework for growing geometries and its application to metal additive manufacturing. It is well-known that virtual part design and qualification in additive manufacturing requires highly-accurate multiscale and multiphysics analyses. Only high performance computing tools are able to handle such complexity in time frames compatible with time-to-market. However, efficiency, without loss of accuracy, has rarely held the centre stage in the numerical community. Here, in contrast, the framework is designed to adequately exploit the resources of high-end distributed-memory machines. It is grounded on three building blocks: (1) Hierarchical adaptive mesh refinement with octree-based meshes; (2) a parallel strategy to model the growth of the geometry; (3) the customization of a parallel iterative linear solver, which leverages the so-called balancing domain decomposition by constraints preconditioning approach for fast convergence and high parallel scalability. Computational experiments consider the heat transfer analysis at the part scale of the printing process by powder-bed technologies. After verification against a 3D benchmark, a strong scaling analysis is carried out for a simulation of 48 layers printed in a cuboid. The cuboid is adaptively meshed to model a layer-by-layer metal deposition process and the average global problem size amounts to 10.3 million unknowns. An unprecedented scalability for problems with growing domains is achieved, with the capability of simulating the printing and recoat of a single layer in 8 seconds average on 3,072 processors. Hence, this framework contributes to take on higher complexity and/or accuracy, not only of part-scale simulations of metal or polymer additive manufacturing, but also in welding, sedimentation, atherosclerosis, or any other physical problem where the physical domain of interest grows in time.*

**Keywords:** Parallel computing, domain decomposition, finite elements, adaptive mesh refinement, additive manufacturing, powder-bed fusion.

## 1. INTRODUCTION

Additive Manufacturing (AM), broadly known as 3D Printing, is introducing a disruptive design paradigm in the manufacturing landscape. The key potential of AM is the ability to cost-effectively create *on-demand* objects with complex shapes and enhanced properties, that are near impossible or impractical to produce with conventional technologies, such as casting or forging. Adoption of AM is undergoing an exponential growth lead by the aerospace, defence, medical and dental industries and the prospect is a stronger and wider presence as a manufacturing technology [70].

Nowadays, one of the main showstoppers in the AM industry, especially for metals, is the lack of a software ecosystem supporting fast and reliable product and process design. Part qualification is chiefly based on slow and expensive trial-and-error physical experimentation and the understanding of the process-structure-performance link is still very obscure. This situation precludes further implementation of AM and it is a call to action to shift to a virtual-based design model, based on predictive computer simulation tools. Only then will it be possible to fully leverage the geometrical freedom, cost efficiency and immediacy of this technology.

---

*Date:* October 26, 2018.

This work addresses the numerical simulation of metal AM processes through *High Performance Computing (HPC) tools*. The mathematical modelling of the process involves dealing with multiple scales in space (e.g. part, melt pool, microstructure), multiple scales in time (e.g. microseconds, hours), coupled multiphysics [27, 43] (e.g. thermomechanics, phase-change, melt pool flow) and arbitrarily complex geometries that grow in time. As a result, high-fidelity analyses, which are vital for part qualification, can be extremely expensive and require vast computational resources. In this sense, HPC tools capable to run these highly accurate simulations in a time scale compatible with the time-to-market of AM are of great importance. By efficiently exploiting HPC resources with scalable methods, one can drastically reduce CPU time, allowing the optimization of the AM building process and the virtual certification of the final component in reasonable time.

Experience acquired in modelling traditional processes, such as casting or welding [21, 22, 50], has been the cornerstone of the first models for metal AM processes [2, 17, 47, 53, 62]. At the part scale, Finite Element (FE) modelling has proved to be useful to assess the influence of process parameters [59], compute temperature distributions [24, 28], or evaluate distortions and residual stresses [30, 52, 61]. Recent contributions have introduced microstructure simulations of grain growth [49, 63] and crystal plasticity [42], melt-pool-scale models [43, 72] and even multiscale and multiphysics solvers [41, 51, 64, 71, 73]. Furthermore, advanced frameworks (e.g. grounded on multi-level *hp*-FE methods combined with implicit boundary methods [46]) or applications to topology optimization [68] have also been considered.

However, in spite of the active scientific progress in the field, the authors have detected that very little effort has turned to the design of *large scale* FE methods for metal AM. Even if computational efficiency has been taken into consideration in several works, all approaches have been limited to Adaptive Mesh Refinement (AMR) [29, 60] or simplifications [25, 35, 36, 65] that sacrifice the accuracy of the model. Scalability has been generally disregarded (with few exceptions [49]), even if it is fundamental to face more complexity and/or provide increased accuracy at acceptable CPU times. For instance, for the high-fidelity melt-pool solver in [72], a simulation of 16 ms of physical time with 7 million cells requires 700 h of CPU time on a common desktop with an Intel Core i7-2600.

The purpose of this work is to design a novel scalable parallel FE framework for metal AM *at the part scale*. Our approach considers three main building blocks:

- (1) *Hierarchical AMR with octree meshes* (see Sect. 2). The dimensions of a part are in the order of [mm] or [cm], but relevant physical phenomena tend to concentrate around the melt pool [ $\mu\text{m}$ ]. Likewise, in powder-bed fusion, the layer size is also [ $\mu\text{m}$ ], i.e. the scale of growth is much smaller than the scale of the part. Hence, adaptive meshing can be suitably exploited for the highly-localized nature of the problem. Here, a parallel octree-based *h*-adaptive FE framework [10] is established.
- (2) *Modelling the growth of the geometry* (see Sect. 3). In welding and AM processes, the addition of material into the part has been typically modelled by adding new elements into the computational mesh. To this effect, the simulation starts with the generation of a *static* background mesh comprising the substrate and the filling, i.e. the final part. At each time step, the elements in the region that has not yet been filled are either assigned penalized properties (*quiet*-element method, which perturbs the original problem) or excluded from the computational domain (*element-birth* method), both detailed in [23, 57]. This work adapts the latter to the parallel hierarchical AMR framework above. In addition, a strategy is devised to balance the computational load among processors, during the growth of the geometry.
- (3) *Adapting a highly scalable parallel iterative linear solver* (see Sect. 4). Compared to sparse direct solvers, iterative solvers can be efficiently implemented in parallel computer codes for distributed-memory machines. However, they must also be equipped with efficient preconditioning schemes to accomplish parallel/algorithmic scalability. To this end, this work relies on nonoverlapping Domain Decomposition (DD) [16, 56, 69], by considering a customization to the problem at hand of the Balancing Domain Decomposition by Constraints (BDDC) method [8].

As the originality of the framework centres upon the computational aspects to efficiently deal with growing geometries, these blocks are presented in an abstract way, i.e. without considering a reference physical problem. Afterwards, Sect. 5 considers an application to the heat transfer analysis of metal AM processes by powder-bed fusion. Nonetheless, the authors believe that the framework can readily be extended to a coupled thermomechanical analysis, adapted to other metal or polymer technologies, or even be useful to other domains of study, such as the simulation of sedimentation processes.

Computer implementation was supported by FEMPAR [12, 13], a general-purpose object-oriented message-passing/multi-threaded scientific software for the fast solution of multiphysics problems governed by partial differential equations. FEMPAR adapts to a range of computing environments, from desktop and laptop computers to the most advanced HPC clusters and supercomputers. On the other hand, it contains an implementation of BDDC that scales up to 458,672 cores on the JUQUEEN supercomputer (JSC, Germany) [9]. The computer implementation of the framework, using this high-end infrastructure, has given rise to the FEMPAR-AM module for FE analyses of metal AM processes.

The numerical study of the framework in Sect. 6 starts with a verification of the thermal FE model against a well-known 3D benchmark. Validation of this heat transfer formulation has already been object of previous works [24, 25] and it is not covered here. A strong scaling analysis follows, with a special focus on sources of load imbalance, identified as a major parallel overhead threatening the efficiency of the implementation, and corresponding corrective measures. A relevant outcome is the capability of simulating the printing of a single layer in a 10 million unknown problem in merely 8 seconds average with 3,072 processors. In conclusion (see Sect. 7), the fully-distributed, parallel framework presented in this work is set to contribute to the efficient simulation of AM processes, a critical aspect long identified, though mostly neglected by the numerical community.

## 2. MESH GENERATION BY HIERARCHICAL AMR

Physical phenomena are often characterized by multiple scales in both space and time. When the smallest scales are highly-localized in the physical domain of analysis, uniformly refined meshes tend to be impractical from the computational viewpoint, even for the largest available supercomputers.

The purpose of AMR is to reach a compromise between the high-accuracy requirements in the regions of interest and the computational effort of solving for the whole system. To this end, the mesh is refined in the regions of the domain that present a complex behaviour of the solution, while larger mesh sizes are prescribed in other areas.

In this work, the areas of interest are known *a priori* and correspond to the growing regions. It is assumed that the geometrical scale of growth is much smaller than the domain of study, as it is the case of welding or AM processes. However, the most usual approach in FE analysis is to drive the AMR with *a posteriori* error estimates [1]. These quantities are cell-wise indicators of approximation error generated from the FE solution to the PDE. Besides, the framework is restricted to *h*-adaptivity, i.e. only the mesh size changes among cells, in contrast to *hp*-adaptivity, where the polynomial order  $p$  of the FEs may also vary among cells. This computational framework is briefly outlined in this section; the reader is referred to [10] for a thorough exposition.

**2.1. Hierarchical AMR with octree meshes.** Let us suppose that  $\Omega \subset \mathbb{R}^d$  is an open bounded polyhedral domain, being  $d = 2, 3$  the dimension of the physical space. Let  $\mathcal{T}_h^0$  be a conforming and quasi-uniform partition of  $\Omega$  into quadrilaterals ( $d = 2$ ) or hexahedra ( $d = 3$ ), where every  $K \in \mathcal{T}_h^0$  is the image of a reference element  $\hat{K}$  through a smooth bijective mapping  $F_K$ . If not stated otherwise, these hypotheses are common to all sections of this document.

Hierarchical AMR is a multi-step process. The mesh generation consists in the transformation of  $\mathcal{T}_h^0$ , typically as simple as a single quadrilateral or hexahedron, into an objective mesh  $\mathcal{T}_h$  via a finite number of refinement/coarsening steps; in other words, the AMR process generates a sequence  $\mathcal{T}_h^0, \mathcal{T}_h^1, \dots, \mathcal{T}_h^m \equiv \mathcal{T}_h$  such that  $\mathcal{T}_h^i = \mathcal{R}(\mathcal{T}_h^{i-1}, \theta^i)$ ,  $i = 1, \dots, m < \infty$ , where  $\mathcal{R}$  applies the refinement/coarsening procedure over  $\mathcal{T}_h^{i-1}$  and  $\theta^i : \mathcal{T}_h^{i-1} \rightarrow \{-1, 0, 1\}$  is an array establishing the action to be taken at each cell: -1 for coarsening, 0 for "do nothing" and 1 for refinement.

A cell marked for refinement is partitioned into four (2D) or eight (3D) children cells by bisecting all cell edges. As a result,  $\mathcal{T}_h$  can be interpreted as a collection of quadtrees (2D) or octrees (3D), where the cells of  $\mathcal{T}_h^0$  are the roots of these trees, and children cells (a.k.a. quadrants or octants) branch off their parent cells. The leaf cells in this hierarchy form the mesh in the usual meaning, i.e.  $\mathcal{T}_h$ . Furthermore, for any cell  $K \in \mathcal{T}_h$ ,  $l(K)$  is the *level* of refinement of  $K$  in the aforementioned hierarchy. In particular,  $l(K) = 0$  for the root cells and  $l(K) = l(\text{parent}(K)) + 1$ , otherwise. The level can also be defined for lower dimensional mesh entities (vertices, edges, faces) as in [37, Def. 2.4]. Fig. 1 illustrates this recursive tree structure with cells at different levels of refinement stemming from a single root.

Octree meshes admit a very compact computer representation, based on Morton encoding [58] by bit interleaving, which enables efficient manipulation in high-end distributed-memory computers [18]. Moreover, they provide multi-resolution capability by local adaptation, as the leaves in the hierarchy can be at different levels of refinement. However, they are potentially nonconforming by construction, e.g. there can be *hanging* vertices in the middle of an edge or face or *hanging* edges or faces in touch with a coarser geometrical entity. Nonconformity introduces additional complexity in the implementation of conforming FEs, especially in parallel codes for distributed-memory computers. This degree of complexity is nevertheless significantly reduced by enforcing the so-called *2:1 balance* relation, i.e. adjacent cells may differ at most by a single level of refinement. In this sense, the mesh in Fig. 1 violates the 2:1 balance, because hanging vertex  $a$  is surrounded by cells that differ by two levels.

**2.2. Imposition of hanging node constraints.** Assuming a conforming discretization with Lagrangian FEs, Degrees of Freedom (DOFs) sitting on *hanging* geometric entities cannot have an arbitrary value, in order to preserve the continuity of the FE approximation. In particular, given a hanging open entity  $F$  (closed, if a vertex) and the open entity  $F'$  such that  $F \subset F'$  and  $\text{lev}(F) = \text{lev}(F') + 1$ , the value  $V_\xi$  of a DOF  $\xi \in F$ , located at the point  $\mathbf{x}_\xi$ , is subject to the constraint

$$V_\xi = \sum_{\chi \in F' \cup \partial F'} \varphi^\chi(\mathbf{x}_\xi) V_\chi, \quad (1)$$

where  $\chi$  are the DOFs belonging to  $F' \cup \partial F'$ ,  $\varphi^\chi(\mathbf{x}_\xi)$  is the value of the shape function associated to  $\chi$  evaluated at  $\mathbf{x}_\xi$ , and  $V_\chi$  is the value of the DOF  $\chi$ . An example of such constraint is also depicted in Fig. 1.

On the other hand, as with constrained DOFs of Dirichlet type, there are two main strategies to handle hanging DOFs. One option is to keep them in the global system and impose additional constraints to ensure continuity. Alternatively, the approach advocated in this work [48] eliminates the hanging node constraints of the local matrices, before assembling the global matrix. In this case, hanging DOFs are not associated to global DOFs and, thus, a row/column in the global linear system of equations.

**2.3. Partitioning the octree mesh.** Efficient and scalable parallel partitioning schemes for adaptively refined meshes are still an active research topic. Our computational framework [10] relies on the **p4est** library [18]. **p4est** is a Message Passing Interface (MPI) library for efficiently handling (forests of) octrees that has scaled up to hundreds of thousands of cores [15]. Using the properties of the Morton encoding, **p4est** offers, among others, parallel subroutines to refine (or coarsen) the octants of an octree, enforce the 2:1 balance ratio and partition/redistribute the octants among the available processors to keep the computational load balanced [18, 37].

The principle underlying its partitioner is the use of space-filling curves. Octants within an octree can be naturally assigned an ordering by a traversal across all leaves, e.g. increasing Morton index, as shown in Fig. 1. Application of the one-to-one correspondence between tree nodes and octants reveals that this one-dimensional sequence corresponds exactly to a  $z$ -order space-filling curve of the triangulation  $\mathcal{T}_h$ . Hence, the problem of partitioning  $\mathcal{T}_h$  can be reformulated into the much simpler problem of subdividing a one-dimensional curve. This circumvents the parallel scaling bottleneck that commonly arises from *dynamic load balancing* via graph partitioning algorithms [38, 39].

However, the simplicity comes at a price related to the fact that, among space-filling curves,  $z$ -curves have unbounded locality and low bounding-box quality [34]. In our context, this leads to the

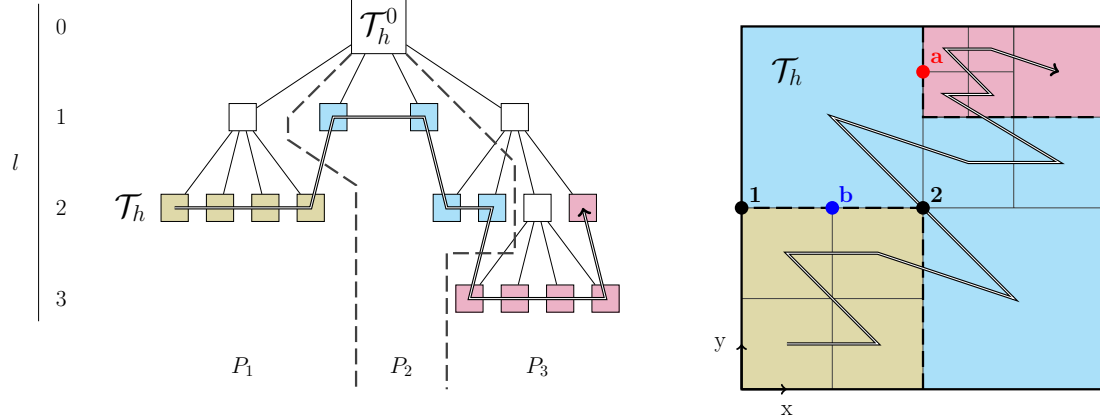


FIGURE 1. The hierarchical construction of  $\mathcal{T}_h$  gives rise to a one-to-one correspondence between the cells of  $\mathcal{T}_h$  and the leaves of a quadtree rooted in  $\mathcal{T}_h^0$ .  $\mathcal{T}_h$  does not satisfy the *2:1 balance*, e.g. the red hanging vertex  $a$  is not permitted. Assuming a discretization with conforming Lagrangian linear FEs, the value of the DOF at hanging vertex  $b$  is subject to the constraint  $V_b = 0.5V_1 + 0.5V_2$ .  $\mathcal{T}_h$  is partitioned into three subdomains,  $P_1$ ,  $P_2$  and  $P_3$ , using the  $z$ -order curve obtained by traversing the leaves of the octree in increasing Morton index. Adapted from [18].

emergence of poorly-shaped and, possibly, disconnected subdomains (with at most two components [19] for single-octree meshes). Bad quality of subdomains affects the performance of nonoverlapping DD methods, such as BDDC [48] (see Sect. 4).

### 3. MODELLING THE GROWTH OF THE GEOMETRY

**3.1. The element-birth method.** As mentioned in Sect. 1, the growth of the geometry is modelled in a *background* FE mesh that, even if it is refined or coarsened, always covers the same domain.

Let  $\Omega(t)$  be a *growing-in-time* domain with the initial hypotheses stated in Sect. 2. During the time interval  $[t_i, t_f]$ ,  $\Omega(t)$  transforms from an initial domain  $\Omega_i$  to a final one  $\Omega_f$ . For the sake of simplicity, AMR is not considered in the following exposition (but it is in the implementation) and it is assumed that there exists (1) a *background* conforming partition  $\mathcal{T}_h \equiv \mathcal{T}_h^0 = \{K\}$  of  $\Omega_f$  and (2) a time discretization  $t_i = t_0 < t_1 < \dots < t_{N_t} = t_f$  such that, for all  $j = 0, \dots, N_t$ , a partition  $\mathcal{T}_{h,j}$  of  $\Omega(t_j)$  can be obtained as a subset of cells of  $\mathcal{T}_h$ . In other words, a body-fitted mesh of  $\Omega_f$  can be built so that subsets of this mesh can be taken as body-fitted meshes of  $\Omega(t_j)$ ,  $j = 0, \dots, N_t$ . As  $\Omega(t)$  grows in time, the relation  $\mathcal{T}_{h,i} = \mathcal{T}_{h,0} \subseteq \mathcal{T}_{h,1} \subseteq \dots \subseteq \mathcal{T}_{h,N_t} = \mathcal{T}_{h,f}$  holds.

This setting is typical in welding or AM simulations. In AM, for instance, it is frequently required that the mesh of the component conforms to the layers. On the other hand, the method presented below can be adapted with little effort to a more general setting, where the growth-fitting requirement is dismissed by resorting to unfitted or immersed boundary methods [14]. In this case,  $\mathcal{T}_h$  is a triangulation of an artificial domain  $\Omega_{\text{art}}$ , such that it includes the final physical domain, i.e.  $\Omega_f \subset \Omega_{\text{art}}$ , but it is also characterized by a simple geometry, easy to mesh with Cartesian grids.

Consider now partitions of  $\mathcal{T}_h$  of the form  $\{\mathcal{T}_{h,j}, \mathcal{T}_h \setminus \mathcal{T}_{h,j}\}$ ,  $j = 0, \dots, N_t$ . In this classification, the cells in  $\mathcal{T}_{h,j}$  are referred to as the *active* cells  $K_{\text{ac}}$ , while the ones in  $\mathcal{T}_h \setminus \mathcal{T}_{h,j}$  as the *inactive* cells  $K_{\text{in}}$ . The key point of the *element-birth* technique is to assign degrees of freedom only in active cells, that is, the computational domain, at any  $j = 0, \dots, N_t$ , is defined by  $\mathcal{T}_{h,j} = \{K_{\text{ac}}\}$ . Note the similarities of this approach to the one employed in unfitted FE methods [6, 14], distinguishing interior and cut (active) cells from exterior (inactive) cells.

This representation of a growing domain is completed with a procedure to update the computational mesh during a time increment. The most usual approach is to use a search algorithm to find the set

of cells in  $\mathcal{T}_{h,j+1} \setminus \mathcal{T}_{h,j}$ ,  $j = 0, \dots, N_t - 1$ , referred to as the *activated* cells  $K_{\text{acd}}$ . Then,  $\mathcal{T}_{h,j+1} = \mathcal{T}_{h,j} \cup \{K_{\text{acd}}\}$  defines the next computational mesh, as illustrated in Fig. 8. This means that  $\mathcal{T}_{h,j+1}$  receives the old DOFs global identifiers (and FE function DOF values) from  $\mathcal{T}_{h,j}$  and has new degrees of freedom assigned in the activated cells. The initial value of these new DOFs is set with a criterion that depends on the application problem, as seen in Sect. 5.

**3.2. Dynamic load balancing.** Assuming from Sect. 2 a single-octree mesh,  $\mathcal{T}_h$  is now a nonconforming triangulation of a voxel domain  $\Omega_{\text{oct}}$ , such that  $\Omega_f \subseteq \Omega_{\text{oct}}$ . Adding to this the element-birth method, there are two different partitions of  $\mathcal{T}_h$  playing a role in the simulation: (1) into subdomains and (2) into active  $K_{\text{ac}}$  and inactive  $K_{\text{in}}$  cells.

When designing a scalable application, (1) must be defined such that it evenly distributes among processors the total computational load. However, to this goal, (2) adds two mutually excluding constraints. Indeed, while the size of data structures and the complexity of procedures that manipulate the mesh grow with the total number of cells, those concerning the FE space, the FE system and the linear solver depend on the number of active cells (i.e. number of DOFs).

The distribution of computational work can be tuned by allowing for a user-specified *weight function*  $w$  that assigns a non-negative integer value to each octant. It follows that the partition is constructed by equally distributing the accumulated weights of the octants that each processor owns, instead of the number of owned octants per processor. As `p4est` provides such capability (see [18, Sect. 3.3]), the remaining question is to decide how to define  $w$ , taking into account the constraints above.

The answer depends on how the computational time is distributed among the different stages of the FE simulation pipeline. In the context of growing domains, the FE analysis is transient and it may be often desirable to reuse the same mesh for several time steps, seeking to minimize the AMR events and, thus, reduce simulation times. In this scenario, the number of time steps (linear system solutions) is greater than the number of mesh transformations and  $w$  should favour the balance of active cells. With this idea in mind, the weight function can be defined as

$$w_K = \begin{cases} w_a & \text{if } K \in \{K_{\text{ac}}\} \\ w_i & \text{if } K \in \{K_{\text{in}}\} \end{cases} \quad (2)$$

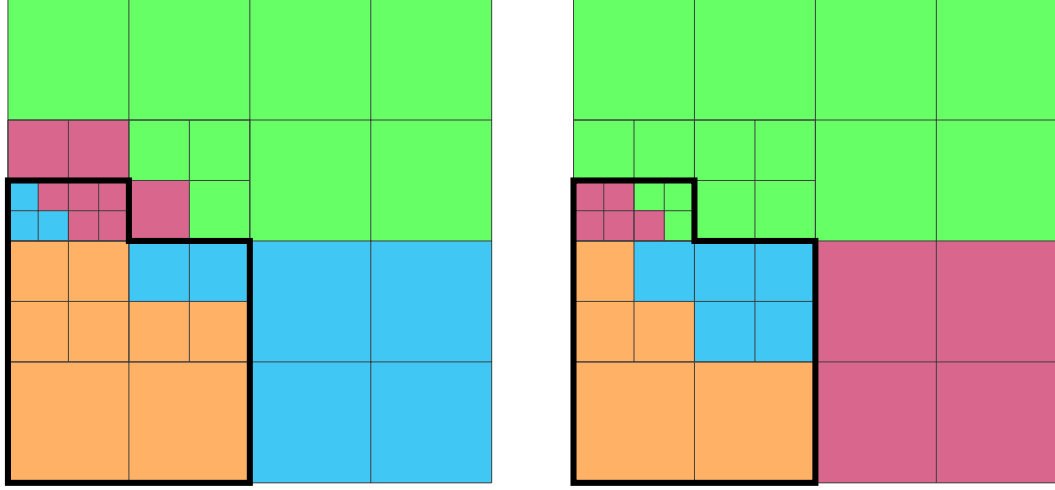
where  $w_a \in \mathbb{N}$  and  $w_i \in \mathbb{N}^0$ .

The effect of this weight function is illustrated in Fig. 2. A uniform distribution of the octree octants,  $(w_a, w_i) = (1, 1)$ , may lead to high load imbalance in the number of DOFs per subdomain. There can even be fully inactive parts, as shown in Fig. 2(a), leaving the processors in charge of them mostly idling during local integration, assembly and solve phases. In contrast,  $(w_a, w_i) = (1, 0)$  gives the most uniform distribution of  $\{K_{\text{ac}}\}$ , but it can also lead to extreme imbalance of  $\{K_{\text{in}}\}$  and, thus, the whole set of triangulation cells. Alternatively, pairs  $(w_a, w_i)$  satisfying  $w_a \gg w_i$  offer good compromise partitions.

#### 4. PARALLEL LINEAR SOLVER

This section introduces the two-level BDDC method for growing domains. The first part in Sect. 4.1 is devoted to briefly describe the BDDC algorithm for conforming meshes, focusing on the linear systems that are required to be solved, as they are brought later again into the discussion of the numerical results in Sect. 6. The reader is referred to [16, 54] for a detailed exposition, to [8, 9] for practical implementation aspects and to [48] for the coupling with AMR. The second part in Sect. 4.2 centres upon the modifications carried out to the standard BDDC preconditioner to deal with growing domains.

**4.1. The two-level BDDC preconditioner.** Assuming, with respect to Sect. 2, that  $\mathcal{T}_h \equiv \mathcal{T}_h^0$  is a *fine* conforming partition into *cells*, let  $\Theta$  be a *coarse* partition of  $\mathcal{T}_h$  into *subdomains*. The *coarse* partition  $\Theta$  induces a nonoverlapping DD of  $\Omega$  into subdomains  $\Omega^i$ ,  $i = 1, \dots, n^{\text{sbd}}$  of characteristic size  $H$ . The interface of  $\Omega^i$  is defined as  $\Gamma^i := \partial\Omega^i \setminus \partial\Omega$ , while the whole interface (skeleton) of the



(A) A default partition, that is,  $(w_a, w_i) = (1, 1)$ , can result in a poor balancing of DOFs and even fully inactive parts (e.g. green subdomain).

(B) By setting partition weights to, e.g.  $(w_a, w_i) = (10, 1)$ , the active cells can be balanced, leading to a more equilibrated parallel distribution of the DOFs.

FIGURE 2. 2D example illustrating how partition weights can be used to balance dynamically the DOFs across the processors. Each colour represents a different subdomain. Active cells are enclosed by a thick contour polygon, representing the computational domain.

DD is  $\Gamma := \bigcup_{i=1}^{n^{sbd}} \Gamma^i$ . The two-level hierarchical nature of this setting is apparent from the fact that the coarse partition overlaps the fine one.

The model problem is the Poisson's equation on  $\Omega$  with homogeneous Dirichlet boundary conditions on  $\partial\Omega$ . Considering  $\bar{\mathbb{V}} \subset H^1(\Omega)$  a conforming Lagrangian FE space,  $\mathbb{V}^i$  denotes the *local* FE spaces, i.e. the restriction of  $\bar{\mathbb{V}}$  into  $\Omega^i \in \Theta$  and  $\mathbb{V} := \mathbb{V}^1 \times \dots \times \mathbb{V}^{n^{sbd}}$  is the global *subassembled* FE space of functions that can be discontinuous across  $\Gamma$ . The Galerkin FE approximation of the continuous problem at hand in  $\bar{\mathbb{V}}$  gives rise to the global linear system of equations

$$Ax = f. \quad (3)$$

The subassembled FE matrices corresponding to  $\mathbb{V}^i$  and  $\mathbb{V}$  are denoted by  $K^i$  and  $K$ . Similarly, the local and global subassembled right-hand sides are defined as  $g^i$  and  $g$ . The system matrix  $A$  and the right-hand side  $f$  are recovered after assembly of  $K$  and  $g$ .

The set of nodes of  $\mathcal{T}_h$  belonging to  $\Gamma$  is denoted by  $\Gamma_h$  and has cardinality  $n_\Gamma$ . Besides, the nonoverlapping partition into subdomains induces a block reordered structure of Eq. (3) that takes the form

$$\begin{bmatrix} A_{II} & A_{I\Gamma} \\ A_{\Gamma I} & A_{\Gamma\Gamma} \end{bmatrix} \begin{bmatrix} x_I \\ x_\Gamma \end{bmatrix} = \begin{bmatrix} f_I \\ f_\Gamma \end{bmatrix}, \quad (4)$$

where  $x_\Gamma$  is the vector of unknowns corresponding to the nodes in  $\Gamma_h$ , while  $x_I$  corresponds to the nodes in the subdomain interiors. Likewise, this structure can be naturally brought to the local and global subassembled matrices and vectors.

The construction of the BDDC preconditioner is grounded on a partition of the DOFs of  $\mathbb{V}$  on the interface  $\Gamma$  into objects, which can be corners, edges or faces [7]. Some (or all) of these objects are associated to a *coarse* DOF. The coarse DOF can be the value of the unknown on the corner or its mean value on the edge/face. The BDDC space  $\tilde{\mathbb{V}}$  is defined as the subspace of functions in  $\mathbb{V}$  that are continuous on coarse DOFs; clearly,  $\bar{\mathbb{V}} \subset \tilde{\mathbb{V}} \subset \mathbb{V}$ .

Therefore, the characterization of the coarse DOFs defines  $\tilde{\mathbb{V}}$  and leads to different variants of the BDDC method. The most common ones are BDDC(c), BDDC(ce) and BDDC(cef), enforcing continuity on only corner coarse DOFs, corner and edge coarse DOFs, and corner, edge and face coarse DOFs, respectively. More generally, for arbitrary partitions and other physical problems, the definition of the objects and the coarse DOFs must ensure the well-posedness of the preconditioner. One may use kernel detection mechanisms [66], modified transmission conditions [4] or face-based schemes [11] for this purpose.

The BDDC preconditioner [69, Ch.2] is of Schwarz-type and it is characterized by a combination of a local interior correction with another global one in the BDDC space  $\tilde{\mathbb{V}}$ . The latter is responsible for coupling all subdomains and endowing scalability and optimality properties. The interior correction operator is defined as  $R_I^t A_{II}^{-1} R_I$ , with  $R_I$  the interior restriction operator  $R_I u_I := u$ . This operator involves the solution of local Dirichlet problems  $(A_{II}^i)^{-1}$ . On the other hand, the BDDC correction in  $\tilde{\mathbb{V}}$  is the Galerkin projection of  $K$  onto  $\tilde{\mathbb{V}}$ , denoted by  $\tilde{K}$ , brought to  $\tilde{\mathbb{V}}$  with an appropriate transfer operator  $B$ , as detailed in [5].

In order to compute the BDDC correction, the BDDC space  $\tilde{\mathbb{V}}$  is decomposed into a *fine* space  $\tilde{\mathbb{V}}_F$  of vectors that vanish on coarse DOFs and the *coarse* space  $\tilde{\mathbb{V}}_C$ , defined as the  $\tilde{K}$ -orthogonal complement of  $\tilde{\mathbb{V}}_F$ . As a result, the FE problem in  $\tilde{\mathbb{V}}$  can be decomposed into fine and coarse components, i.e.  $\tilde{x} = x_F + x_C$ . By  $\tilde{K}$ -orthogonality of the decomposition, these components can be computed in parallel and  $\tilde{K}^{-1} = K_F^{-1} + K_C^{-1}$  holds. In particular, the two-level algorithm can be formulated such that the coarse duties can be isolated [8] in a single *coarse* processor, apart from the *fine* ones.

Since coarse DOFs are the only ones coupling subdomains and they are fixed (to zero) in  $\tilde{\mathbb{V}}_F$ , the set-up of  $K_F^{-1}$  only involves the solution of local Neumann problems  $(K_F^i)^{-1}$  with constrained values at the coarse DOFs belonging to the subdomain. The expression of this linear system reads

$$\begin{bmatrix} K_{II}^i & K_{I\Gamma}^i & 0 \\ K_{\Gamma I}^i & K_{\Gamma\Gamma}^i & C_i^t \\ 0 & C_i & 0 \end{bmatrix} \begin{bmatrix} x_I^i \\ x_\Gamma^i \\ \lambda \end{bmatrix} = \begin{bmatrix} 0 \\ r^i \\ 0 \end{bmatrix}, \quad (5)$$

where the local matrix of constraints  $C_i \in \mathbb{R}^{n_{cts}^i \times n_\Gamma^i}$  returns the local coarse DOF values, when applied to the local vector of interface unknowns.

As for the coarse correction,  $\tilde{\mathbb{V}}_C \subset \tilde{\mathbb{V}}$  is built as  $\tilde{\mathbb{V}}_C = \text{span}\{\phi^1, \phi^2, \dots, \phi^{n_{cts}^i}\}$ , with  $\phi^\alpha \in \tilde{\mathbb{V}}_C$  defined as the *coarse shape function* associated to the coarse DOF  $\alpha$ , i.e. it takes value one on  $\alpha$  and vanishes on the rest of coarse DOFs. The computation of  $\phi^\alpha, \alpha = 1, \dots, n_{cts}^i$ , follows also from solving local constrained Neumann problems  $(K_F^i)^{-1}$ . In this case, the linear system has as many right-hand sides as coarse DOFs in the subdomain and it takes the form

$$\begin{bmatrix} K_{II}^i & K_{I\Gamma}^i & 0 \\ K_{\Gamma I}^i & K_{\Gamma\Gamma}^i & C_i^t \\ 0 & C_i & 0 \end{bmatrix} \begin{bmatrix} \Phi_I^i \\ \Phi_\Gamma^i \\ \Lambda^i \end{bmatrix} = \begin{bmatrix} 0 \\ 0 \\ I_{n_{cts}^i} \end{bmatrix}, \quad (6)$$

where  $\Phi_I^i, \Phi_\Gamma^i$  have  $n_{cts}^i$  columns. The subassembled coarse matrix  $K_C$  is then defined by assembly of the local subdomain matrices  $K_C^i = \Phi_i^t K^i \Phi_i^i$ , for  $i = 1, \dots, n^{sbd}$ . As a result, the two-level BDDC preconditioner can be expressed in compact form as

$$M^{\text{BDDC}} := R_I^t A_{II}^{-1} R_I + B (\Phi A_C^{-1} \Phi^t + K_F^{-1}) B^t, \quad (7)$$

where the coarse problem  $A_C^{-1}$  is solved in the coarse processor.

**4.2. Removing redundant coarse DOFs.** As pointed out in Sect. 2, partitions derived from a  $z$ -order curve can be arbitrarily irregular. In the case of growing domains, the irregularity is more prominent when the growth scale is smaller than the domain scale and there is an aggressive coarsening from the small cells in the growing region to the ones away from it. There can even exist subdomains that are in contact to (almost) all the remaining subdomains, as shown in Fig. 3. In this work, these subdomains are referred to as *(quasi)dominating*.

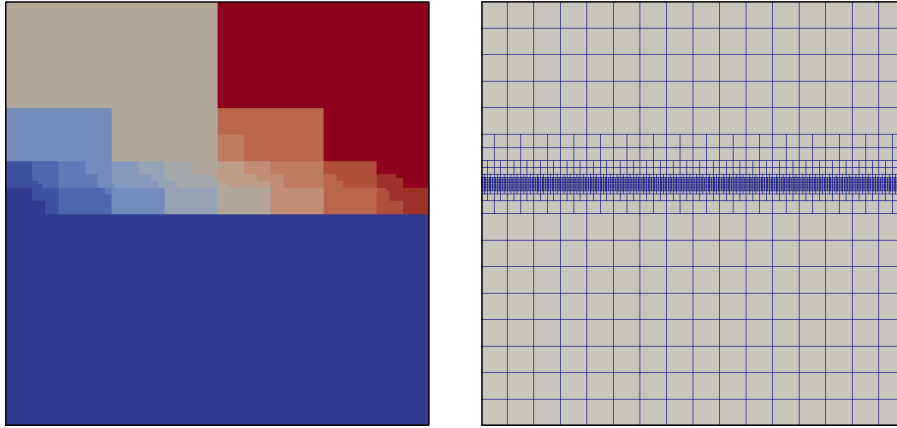


FIGURE 3. Partition and mesh obtained after recursive refinement at a thin band located at the bottom of the top half of the square. As observed, the bottom dark blue subdomain touches almost all other subdomains. This scenario can appear when dealing with growing domains, when small growth scales and aggressive coarsening are present.

This scenario reduces significantly the efficiency and scalability of common variants of the BDDC method. Indeed, a quasidominating subdomain will concentrate a large number of corner-, edge-, or face-connections to other subdomains. As a result, it will also have a large number of local coarse DOFs. Then, recovering Eq. (6), the setup of the coarse basis is expensive (since the number of local coarse DOFs equals the number of right-hand sides for the constrained Neumann problem) and it is also subject to a significant load imbalance among processors.

A heuristic grounded on graph theory and inspired by the BDDC concept of *acceptable path* (see [69, Def. 6.26] and [44, 45]) has been devised to alleviate this issue. The key point concerning acceptable paths (see [11, Th. 3.10]) is that *not all objects need to be associated a coarse DOF to guarantee robustness and optimality of the BDDC method*, i.e. some of the coarse DOFs are redundant. According to this, the goal is to bring the number of coarse DOFs of quasidominating subdomains below a threshold, while keeping all neighbours coupled through a sufficiently short path of coarse DOFs.

This approach is better formulated as a graph problem: *Given the ordered pair  $G = (V, E)$ , comprising a set  $V$  of vertices (subdomains) together with a set of  $E$  edges (couplings via coarse DOFs), find a subgraph  $G' = (V, E')$  with  $E' \subseteq E$ , the minimum set such that*

- (C1) *The maximum degree  $\Delta(G')$  of  $G'$  is below a target value  $\Delta^{\max}$ , i.e.  $\Delta(G') \leq \Delta^{\max}$ ;*
- (C2) *Given  $\nu_a, \nu_b \in V$ , the distance in  $G'$  of  $G$ -adjacent vertices is bounded by  $d^{\max}$ , i.e., if  $d_G(\nu_a, \nu_b) = 1$ , then  $d_{G'}(\nu_a, \nu_b) \leq d^{\max}$ .*

Note that the solution of the problem, if it exists, needs not be unique.

Alg. 1 and Figs. 5(a)-5(h) describe the heuristic step-by-step for BDDC(f), that is, enforcing continuity only on faces. In presence of disconnected subdomains, a vertex is assigned to each connected component. BDDC(f) is chosen because it is readily well-posed, without the need to resort to complex kernel detection mechanisms [11]. In addition, its set of coarse DOFs is smaller, compared to, for instance, BDDC(ce) and BDDC(cef).

The input parameters of the algorithm are the graph  $G$  of the coarse DOFs, the maximum allowed degree  $\Delta^{\max}$  and the maximum allowed distance  $d^{\max}$ . The algorithm runs on the coarse processor; this means that  $G$  has been built by gathering the *local* graph of coarse DOFs of the fine processors with interprocessor communication. Once  $G'$  is constructed, it is scattered across the fine processors to update the local graph of coarse DOFs.

In order to build  $G'$ , Alg. 1 starts with  $G' = G$  and an empty set of visited vertices  $M$ .  $G'$  is then iteratively transformed, until (C1) is satisfied (Line 3). At each iteration (Lines 4-16), a node with

maximum degree  $\nu_{\max}$  is visited and  $G'$  is *locally* updated, by reducing the number of outgoing edges of  $\nu_{\max}$ , while complying with **(C2)**. In particular, the heuristic proceeds as follows:

- (1) A vertex with maximum degree  $\nu_{\max}$ , i.e.  $\Delta(\nu_{\max}) = \Delta(G')$ , is selected (Line 4 and Fig. 5(b)). If the vertex has already been visited, i.e. it belongs to  $M$ , this means that all of its redundant edges have already been removed and the remaining edges are necessary to preserve **(C2)**. Hence, it is not possible to further decrease  $\Delta(G')$  and the algorithm stops before satisfying **(C1)** (Lines 5-7).
- (2) Since the graph transformations are *local*, there must be a procedure to determine if an outgoing edge of  $\nu_{\max}$  must be kept to comply *globally* with **(C2)**. This procedure (in Line 8, Alg. 2 and Fig. 5(g)) consists of finding the so-called set of *locked* vertices  $L$ . If  $\nu \in L$  and  $(\nu, \nu_{\max}) \in E'$ , then  $(\nu, \nu_{\max})$  cannot be removed without violating **(C2)**. As described in Alg. 2,  $L$  is the union of two different sets  $S, T \subseteq V$ . A vertex  $\nu \in V$  adjacent to  $\nu_{\max}$  in  $G'$  satisfies
  - (a)  $\nu \in S$ , if there exists  $\nu' \in M$  with  $d_G(\nu, \nu') = 1$  and  $d_{G'}(\nu, \nu') \leq d^{\max}$ , but all the paths in  $G'$  from  $\nu$  to  $\nu'$  of length  $\leq d^{\max}$  pass through  $\nu_{\max}$  (Lines 3-10 and Fig. 4(a)).
  - (b)  $\nu \in T$ , if they are in a shortest path in  $G'$  from  $\nu_{\max}$  to  $\nu'$ , where  $\nu' \in M$  and  $\nu_{\max}$  and  $\nu'$  are  $G$ -adjacent, i.e.  $d_G(\nu_{\max}, \nu') = 1$  (Lines 11-13 and Fig. 4(b)). In particular,  $\nu' \in T$  if  $d_{G'}(\nu_{\max}, \nu') = 1$ . Also, note that it suffices to add  $\nu$  to  $T$  only along a single shortest path from  $\nu_{\max}$  to  $\nu'$ .
- (3) A  $(d^{\max}, d^{\max} - 1)$ -ruling set<sup>1</sup>  $R$  of the subgraph  $H \subseteq G'$  formed by the neighbours of  $\nu_{\max}$  in  $G'$  is constructed with a greedy sequential algorithm (Lines 9-10 and Figs. 5(c)-5(d)).  $R$  is a minimal subset of vertices of  $H$  such that any other vertex of  $H$  is at distance  $d^{\max} - 1$ . Hence,  $\{\text{neighbours}(G', \nu_{\max}) \setminus R\}$  is a maximal subset of vertices, whose  $G$ -adjacency to  $\nu_{\max}$  is *locally* redundant.
- (4) Any pair  $(\nu, \nu_{\max}) \in E'$ , such that  $\nu \notin (L \cup R)$  is both *globally* and *locally* redundant and it is removed from  $G'$  (Lines 11-15 and Figs. 5(e)). Finally  $\nu_{\max}$  is added to the set  $M$  of visited vertices (Line 16).

The procedure of Alg. 1 does not generally find the optimal solution. Sometimes it even stops before complying with **(C1)**, as it cannot proceed further without violating **(C2)**. In spite of this, it is still able to control quasidominating subdomains. The result is an improved BDDC method, with better scalability and faster runtime, while keeping robustness (i.e. number of linear solver iterations) untouched, as shown in Sect. 6.2.



(a)  $\nu \in S$ :  $d_G(\nu, \nu') = 1$  and  $d_{G'}(\nu, \nu') \leq d^{\max}$ . (b)  $\nu \in T$ :  $d_G(\nu_{\max}, \nu') = 1$  and  $d_{G'}(\nu_{\max}, \nu') \leq d^{\max}$ .

FIGURE 4. 2D example illustrating the two types of vertices belonging to the set  $L = S \cup T$  of locked vertices for  $d^{\max} = 3$ .  $G$  comprises the solid and dashed edges, whereas  $G'$  only the solid edges. In both situations, if the edge  $(\nu, \nu_{\max})$  is removed, then  $d_{G'}(\nu, \nu_{\max}) > d^{\max}$ , and thus, **(C2)** is violated.

<sup>1</sup>An  $(\alpha, \beta)$ -ruling set [3] of a graph  $G = (V, E)$  is a subset  $W \subseteq V$ , such that any two vertices in  $W$  are at distance at least  $\alpha$  and, for every vertex  $\nu \in V \setminus W$ , there exists a vertex in  $W$  within distance  $\beta$ . For instance, a  $(2, 1)$ -ruling set, commonly known as *maximal independent set*, is a set of non-adjacent vertices that is also maximal, i.e. you cannot add any other non-adjacent vertex to the set.

**Algorithm 1: remove\_redundant\_coarse\_dofs( $G = (V, E), \Delta^{\max}, d^{\max}$ )**


---

```

1  $G' \leftarrow \text{copy}(G)$ 
2  $M \leftarrow \emptyset$  /* M is the set of vertices with maximum degree selected at previous iterations */
3 while  $\Delta(G') > \Delta^{\max}$  do /* loop while constraint (C1) is not satisfied */
4    $\nu_{\max} \leftarrow \text{find\_vertex\_with\_maximum\_degree}(G')$ 
5   if  $\nu_{\max} \in M$  then
6     return  $G'$  /* algorithm stops:  $\nu_{\max}$  previously treated; no more edges from  $\nu_{\max}$  can be removed */
7   end
8    $L \leftarrow \text{find\_locked\_vertex\_set}(G, G', M, \nu_{\max}, d^{\max})$  /* see Alg. 2. */
9    $H \leftarrow \text{subgraph}(G', \text{neighbours}(G', \nu_{\max}))$ 
10   $R \leftarrow \text{find\_ruling\_vertex\_set}(H, \alpha = d^{\max}, \beta = d^{\max} - 1)$ 
11  for  $\nu_i \in \text{neighbours}(G', \nu_{\max}), i = 1, \dots, \Delta_{G'}(\nu_{\max})$  do
12    if  $\nu_i \notin L \cup R$  then
13       $\text{remove\_edge}(G', (\nu_{\max}, \nu_i))$  /*  $(\nu_{\max}, \nu_i)$  is a redundant edge */
14    end
15  end
16   $M \leftarrow M \cup \{\nu_{\max}\}$ 
17 end
18  $G \leftarrow G'$ 

```

---

**Algorithm 2:  $L \leftarrow \text{find\_locked\_vertex\_set}(G, G', M, \nu_{\max}, d^{\max})$** 


---

```

1  $S \leftarrow \emptyset; T \leftarrow \emptyset$ 
2 for  $\nu_i \in M, i = 1, \dots, |M|$  do
3   if  $d_{G'}(\nu_i, \nu_{\max}) < d^{\max}$  then
4     /* find S, i.e. G-adjacent  $\nu_j$  of  $\nu_i$  s.t.  $d_{G'}(\nu_i, \nu_j) \leq d^{\max}$  only through paths containing  $\nu_{\max}$  */
5     for  $\nu_j \in \text{neighbours}(G, \nu_i), j = 1, \dots, \Delta_G(\nu_i)$  do
6        $H \leftarrow \text{subgraph}(G', V \setminus \{\nu_{\max}\})$ 
7       if  $d_H(\nu_i, \nu_j) > d^{\max}$  then
8          $S \leftarrow S \cup \{\text{shortest\_path\_vertex\_set}(G', \nu_i, \nu_j) \cap \text{neighbours}(G', \nu_{\max})\}$ 
9       end
10      end
11    end
12    if  $\nu_i \in \text{neighbours}(G, \nu_{\max})$  then
13       $T \leftarrow T \cup \{\text{shortest\_path\_vertex\_set}(G', \nu_i, \nu_{\max}) \cap \text{neighbours}(G', \nu_{\max})\}$ 
14    end
15   $L \leftarrow S \cup T$ 

```

---

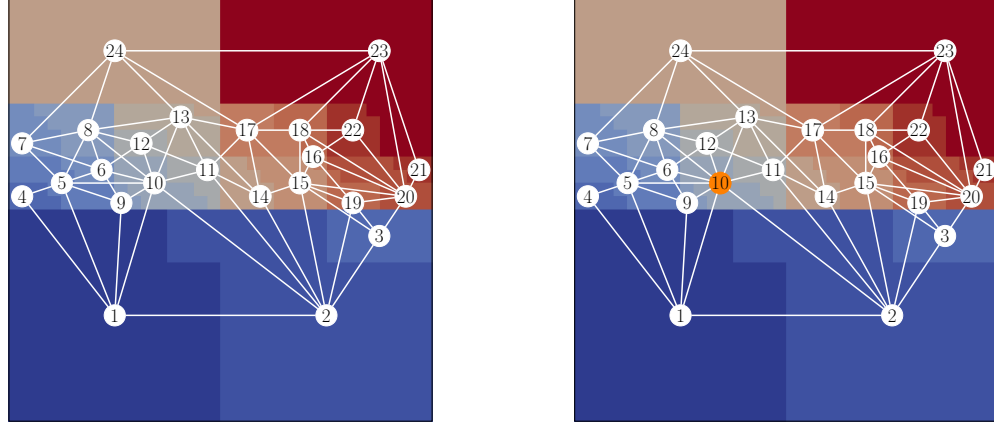
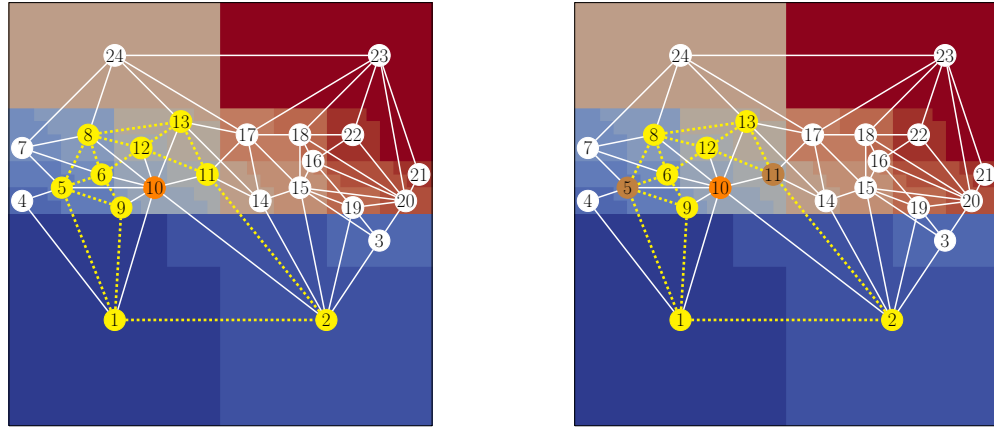
## 5. APPLICATION TO METAL AM

**5.1. Heat transfer analysis.** After introducing the ingredients of the parallel FE framework for growing geometries, the purpose now is to apply it to the thermal analysis of an additive manufacturing process by powder-bed fusion, such as Direct Metal Laser Sintering (DMLS). This manufacturing technology is illustrated in Fig. 6. This will be the reference problem for the subsequent analysis with numerical experiments.

Let  $\Omega(t)$  be a *growing* domain in  $\mathbb{R}^3$  as in Sect. 3. Here,  $\Omega(t)$  represents the component to be printed. The governing equation to find the temperature distribution  $u$  in time is the balance of energy equation, expressed as

$$C(u)\partial_t u - \nabla \cdot (k(u) \nabla u) = f, \quad \text{in } \Omega(t), \quad t \in [t_i, t_f], \quad (8)$$

where  $C(u)$  is the heat capacity coefficient,  $k(u) \geq 0$  is the thermal conductivity and  $f$  is the rate of energy supplied to the system per unit volume by the moving laser.  $C(u)$  is given by the product of the density of the material  $\rho(u)$  and the specific heat  $c(u)$ , but one may consider a modified heat

(a) Build  $G$  the graph of BDDC(f) coarse DOFs.(b) Select vertex  $v_1$  with maximum degree (see Alg. 1 at Lines 5-7).(c) Build  $H = \text{subgraph}(G', \text{neighbours}(G', v_1))$  (see Alg. 1 at Line 9).(d) Find a  $(d^{\max}, d^{\max} - 1)$ -ruling set  $R$  of  $H$  (see Alg. 1 at Line 10, vertices in  $R$  marked in brown).FIGURE 5. 2D example with BDDC(f) describing step-by-step the algorithm to reduce the number of redundant coarse DOFs.  $\Delta^{\max} = 6$  and  $d^{\max} = 2$ . Cont. in Fig. 5(e).

capacity coefficient to also account for phase change effects [25] or compute  $C(u)$  with the CALPHAD approach [40, 41, 67].

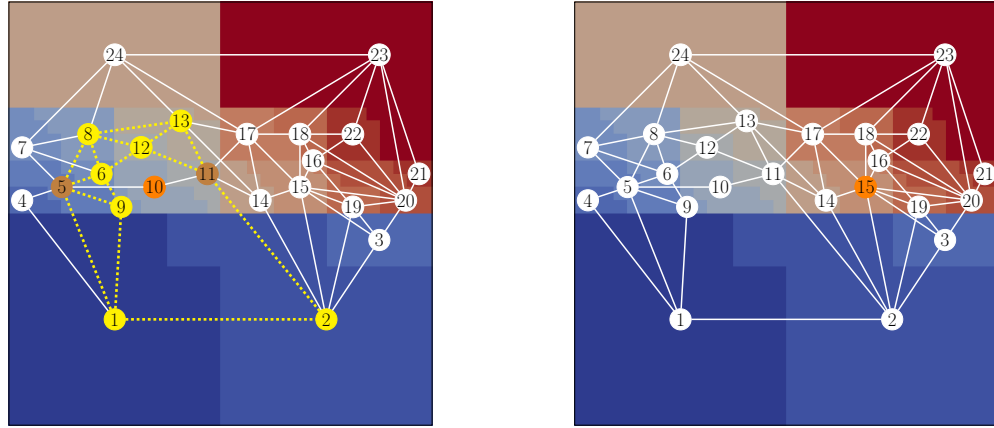
Eq. (8) is subject to the initial condition

$$u(\mathbf{x}, t_i) = u^0(\mathbf{x}) \quad (9)$$

and the boundary conditions described in Fig. 7: (1) heat conduction through the building platform, (2) heat conduction through the powder-bed and (3) heat convection and radiation through the free surface. After linearising the Stefan-Boltzmann's law for heat radiation [24], all heat loss boundary conditions admit a unified expression in terms of Newton's law of cooling:

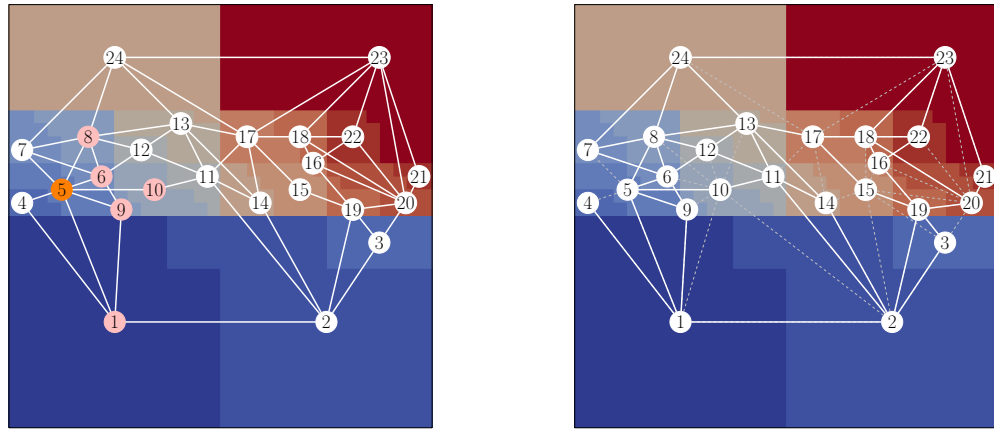
$$q_{\text{loss}}(u, t) = h_{\text{loss}}(u)(u - u_{\text{loss}}(t)), \quad \text{in } \partial\Omega^{\text{loss}}(t), \quad t \in [t_i, t_f], \quad (10)$$

where *loss* refers to the kind of heat loss mechanism (conduction through solid, conduction through powder or convection and radiation) and the boundary region where it applies (contact with building platform, interface solid-powder or free surface).



(E) Remove edges from  $\nu_1$  to  $\text{neighbours}(G', \nu_1) \setminus R$  (see Alg. 1 at Lines 11-15).

(F) Select next vertex  $\nu_2$  and repeat (C-E).



(G) Before repeating (C-E), lock vertices (in pink) whose edges cannot be *globally* removed by **C2** (see Alg. 1 at Line 8 and Alg. 2).

(H) Repeat until **C1** holds or  $\nu_n$  has all neighbours locked by **C2**.

FIGURE 5. 2D example with BDDC(f) describing step-by-step the algorithm to reduce the number of redundant coarse DOFs.  $\Delta^{\max} = 6$  and  $d^{\max} = 2$ . Cont. from Fig. 5(d).

The weak form of the problem defined by Eqs. (8)-(10) can be stated as: *Find  $u(t) \in \mathcal{V}_t = H^1(\Omega(t))$ , almost everywhere in  $(t_i, t_f]$ , such that*

$$(C(u)\partial_t u, v) - (k(u)\nabla u, \nabla v) + \langle h_{\text{loss}}(u)u, v \rangle_{\partial\Omega^{\text{loss}}} = \langle f, v \rangle + \langle h_{\text{loss}}(u)u_{\text{loss}}, v \rangle_{\partial\Omega^{\text{loss}}}, \quad \forall v \in \mathcal{V}_t. \quad (11)$$

Considering now  $\mathcal{T}_h$  the triangulation of  $\Omega_f$ ,  $V_h \subset \mathcal{V}_{t_f}$  a conforming FE space for the temperature field and  $\{\varphi_j(\mathbf{x})\}_{j=1}^{N_h}$  a FE basis of the space  $V_h$ , the semi-discrete form of Eq. (11), after discretization in space with the Galerkin method and integration in time, e.g. with the semi-implicit backward Euler method, reads

$$\begin{aligned} \left[ \frac{\mathbf{M}_C^n}{\Delta t^{n+1}} + \mathbf{A}^n + \mathbf{M}_{\text{loss}}^n \right] \mathbf{U}^{n+1} &= \mathbf{b}_f^{n+1} + \frac{\mathbf{M}_C^n}{\Delta t^{n+1}} \mathbf{U}^n + \mathbf{b}_{\text{loss}}^n, \\ \mathbf{U}(0) &= \mathbf{U}^0, \end{aligned} \quad (12)$$

where the time interval of interest  $[t_i, t_f]$  has been divided in subintervals  $t_i = t_0 < t_1 < \dots < t_{N_t} = t_f$  with  $\Delta t^{n+1} = t_{n+1} - t_n$  variable for  $n = 0, \dots, N_t - 1$ . As a result of using the *element-birth* method

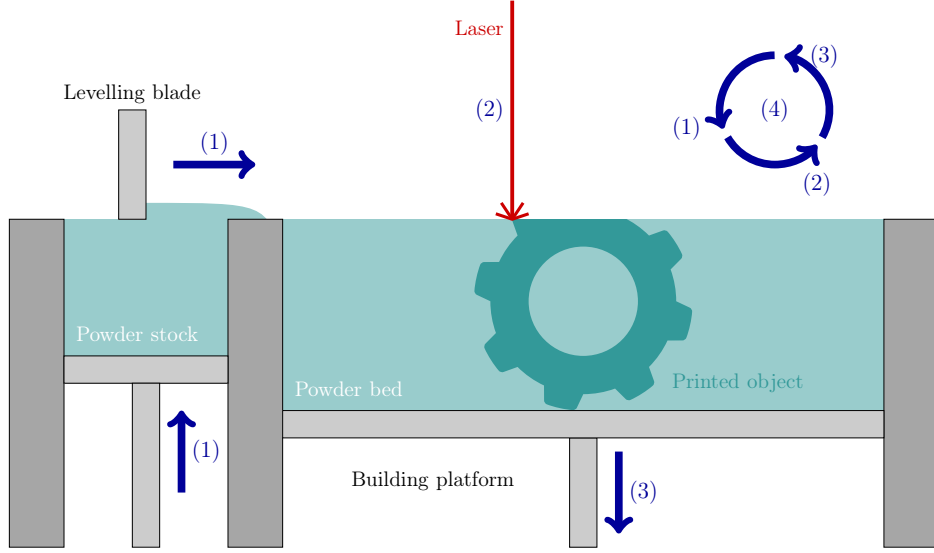


FIGURE 6. A printing process by DMLS. (1) A new layer of powder, around 30-60 microns thick, is spread over the building platform with the levelling blade. (2) A high-energy and focused laser melts the region of powder that belongs to the current cross section of the object. The laser moves according to a predefined *scanning path*. (3) The building platform is lowered to accommodate a new layer. (4) Steps 1. to 3. are repeated until the whole model is created. (5) Loose unfused powder is removed during post processing.

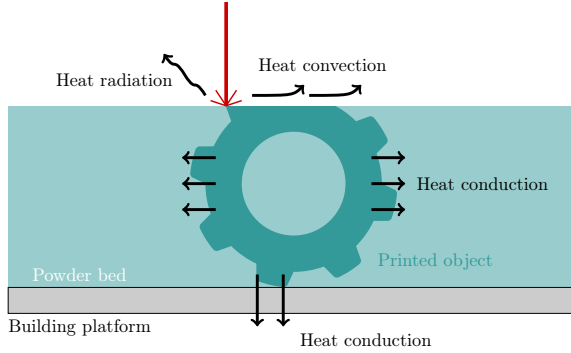


FIGURE 7. A close-up of Fig. 6 gathering the boundary conditions of the problem: (1) Heat conduction through the building platform. (2) Heat conduction through the powder bed. (3) Heat convection and heat radiation through the free surface.

(Sect. 3), Eq. (12) is only constructed in  $\Omega(t_n)$ ,  $n = 0, \dots, N_t - 1$ . In other words, local integration and assembly of Eq. (11) is only carried out at the subset of active elements  $\{K_{ac}\} = \mathcal{T}_{h,n}$ .

Moreover,  $\mathbf{U}(t) = (\mathbf{U}_j(t))_{j=1}^{N_h}$  and  $\mathbf{U}^0 = (\mathbf{U}_j^0)_{j=1}^{N_h}$  are the components of  $\mathbf{U}_h(t)$  and  $\mathbf{U}_h^i$  with respect to the basis  $\{\varphi_j(\mathbf{x})\}_{j=1}^{N_h}$ , and the coefficients of  $\mathbf{M}_\square$ ,  $\mathbf{A}$  and  $\mathbf{b}_\square$  are given by:

$$\begin{aligned} M_C^{n,ij} &= (C(\mathbf{U}^n)\varphi_i, \varphi_j)_{\Omega(t_n)}, \quad M_{\text{loss}}^{n,ij} = \langle h_{\text{loss}}(\mathbf{U}^n)\varphi_i, \varphi_j \rangle_{\partial\Omega^{\text{loss}} \cap \partial\Omega(t_n)}, \quad A^{n,ij} = (k(\mathbf{U}^n)\nabla\varphi_i, \nabla\varphi_j)_{\Omega(t_n)} \\ \mathbf{b}_f^{n+1,i} &= \langle \varphi_i, f^{n+1} \rangle_{\Omega(t_n)}, \quad \mathbf{b}_{\text{loss}}^{n,i} = \langle h_{\text{loss}}(\mathbf{U}^n)\varphi_i, \mathbf{U}_{\text{loss}}(t^{n+1}) \rangle_{\partial\Omega^{\text{loss}} \cap \partial\Omega(t_n)}. \end{aligned}$$

**5.2. FE modelling of the moving thermal load.** As pointed out in Eq. (8),  $f$  is a moving thermal load that models the action of the laser in the system. But the moving heat source also drives the growth of the geometry in time, as the sintering process triggered by the laser transforms the metal powder into new solid material.

Therefore, the FE modelling of the printing process requires a method to apply the volumetric heat source  $f$  in space and time and track the growing  $\Omega(t)$ . The *element-birth* method presented here can serve both purposes, as seen in Fig. 8. In this case, the set of activated cells  $K_{\text{acd}}$ , representing the incremental growth region, is also affected by the laser during the time increment, i.e. the heat source term is also integrated in these cells.

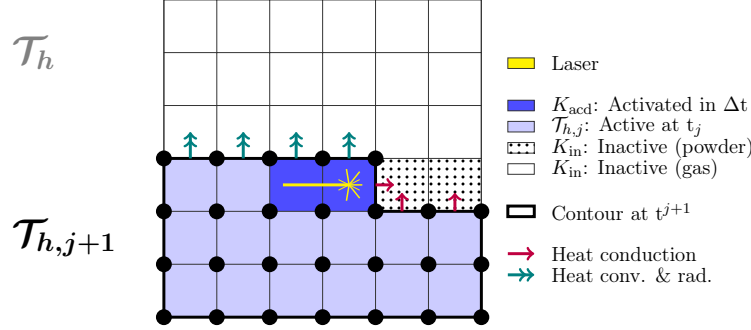


FIGURE 8. Illustration of the *element-birth* method applied to the thermal simulation of an AM process. As shown with this 2D FE cartesian grid, for any  $j = 0, \dots, N_t$ , DOFs are only assigned to the set of active cells  $\{K_{\text{ac}}\} = \mathcal{T}_{h,j+1}$ . A search algorithm is employed to identify the set of activated cells  $\{K_{\text{acd}}\} = \mathcal{T}_{h,j+1} \setminus \mathcal{T}_{h,j}$ , where the laser is focused during  $\Delta t$ . The computational mesh is then updated, by assigning new DOFs in  $K_{\text{acd}}$ . Afterwards, the energy input, as stated by Eq. (13), is uniformly distributed over  $K_{\text{acd}}$ .

Another comment arises on the update of the computational mesh. In general, one aims to follow the actual path of the laser in the machine, as faithfully as possible. Therefore, a search algorithm is needed. It can use the information of the laser path, together with other process parameters, such as the width of the laser, to find the cells affected by the energy input during the time step [24].

However, only layer-by-layer FE activations are considered in Sect. 6. In this case, the identification of the activated cells is trivial. Moreover, it is not necessary to resort to an accurate gaussian heat input model. Hence,  $f$  is taken as a uniform heat source with (average) density distribution computed as

$$f = \frac{\eta W}{V_{\text{layer}}}, \quad (13)$$

where  $W$  is the laser power [watt] and  $\eta$  is the heat absorption coefficient, a measure of the laser efficiency. On the other hand, the initial temperature of the new DOFs is set to the same value as the initial value at the building platform. More accurate alternatives are analysed in the literature [57], but this aspect of the model is not relevant to the overall performance of the framework.

## 6. NUMERICAL EXPERIMENTS AND DISCUSSION

**6.1. Verification of the thermal FE model.** First, the thermal FE model presented in Sect. 5 is verified against a 3D benchmark present in the literature [32, 46] that considers a moving single-ellipsoidal heat source on a semi-infinite solid with null fluxes at the free surface.

Assuming an Eulerian frame of reference  $(x, y, z)$ , consider a heat source located initially at  $z = 0$  that travels at constant velocity  $v$  along the  $x$ -axis on top of the semi-infinite solid defined by  $z \leq 0$ .

The heat source distribution, derived from Goldak's double-ellipsoidal model [33], is defined by

$$q(x, y, z, t) = \frac{6\sqrt{3}}{\pi\sqrt{\pi}} \frac{Q}{abc} \exp \left[ -3 \left( \frac{(x-vt)^2}{a^2} + \frac{y^2}{b^2} + \frac{z^2}{c^2} \right) \right], \quad (14)$$

where  $Q$  is the (effective) rate of energy supplied to the system,  $v$  is the velocity of the laser and  $a, b, c$  are the main dimensions of the ellipsoid, as shown in Fig. 9(a).

The problem at hand is linear and admits a semi-analytical solution using Green's functions [20, 26] given by

$$u(x, y, z, t) = u_0 + \frac{6\sqrt{3}}{\pi\sqrt{\pi}} \frac{\alpha Q}{k} \int_0^t \frac{\exp \left[ -3 \left( \frac{(x-vt)^2}{a^2+12\alpha(t-\tau)} + \frac{y^2}{b^2+12\alpha(t-\tau)} + \frac{z^2}{c^2+12\alpha(t-\tau)} \right) \right]}{\sqrt{(a^2+12\alpha(t-\tau))(b^2+12\alpha(t-\tau))(c^2+12\alpha(t-\tau))}} d\tau, \quad (15)$$

with  $u_0$  the initial temperature and  $\alpha = k/\rho c$  the thermal diffusivity.

Using the symmetry of the problem, the numerical simulation considers a cuboid with coordinates given in Fig. 9(b). The path of the laser follows a segment centred along the edge of the cuboid that sits on the  $x$ -axis. Null fluxes apply at the top surface and the lateral face of symmetry, whereas Dirichlet boundary conditions apply at the remaining contour surfaces to account for the semi-infinite solid.

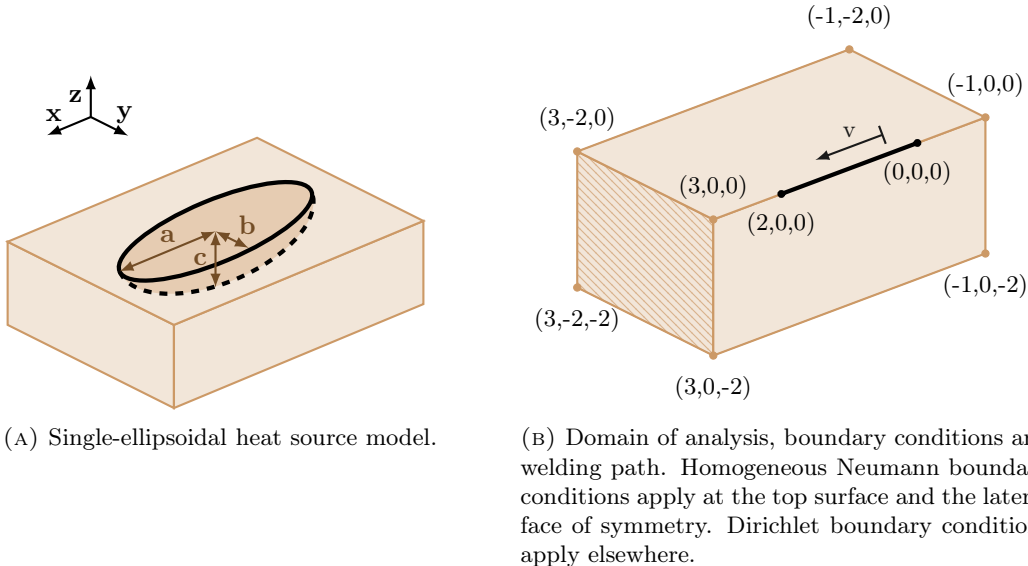


FIGURE 9. 3D semi-analytical benchmark problem. Heat source distribution, geometry and boundary conditions.

An  $h$ -adaptive linear FE mesh is employed, where the smallest size is prescribed around the welding path. Starting with the initial mesh shown in Fig. 10(a) and assigning  $u_0 = 20$ ,  $Q = 50$ ,  $v = 1$ ,  $\alpha = 0.1$ ,  $k = 1$  and  $(a, b, c) = (0.3, 0.15, 0.25)$ , a convergence test is carried out.

For a parabolic heat equation with sufficiently smooth solution, the error in  $L^2([0, T]; H_0^1(\Omega))$  with a Backward Euler time integration scheme is proportional to  $(h^p + \Delta t)$  (see Theorem 6.29 in [31]), where  $p$  is the order of the FE. Since  $p = 1$  in this experiment, the time discretization should be refined at the same rate of the space discretization.

Taking this into consideration with an initial time step of  $\Delta t = 0.008$ , Fig. 11 shows that the numerical error in  $L^2([0, T]; H_0^1(\Omega))$  of the 3D semi-analytical benchmark decreases at the same rate as the theoretical one. This indicates a correct implementation of the thermal FE model.

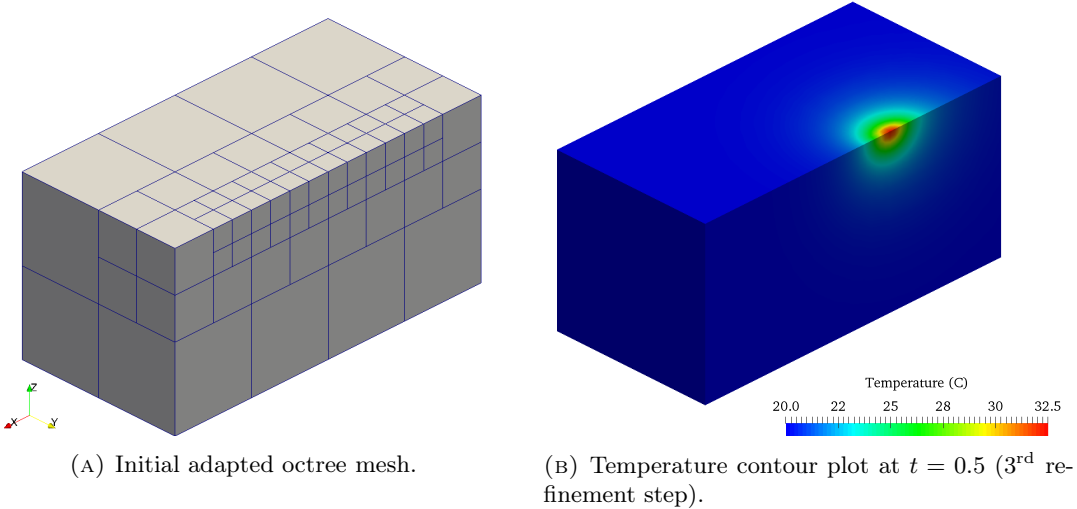


FIGURE 10. 3D semi-analytical benchmark problem. Initial mesh and contour plot.

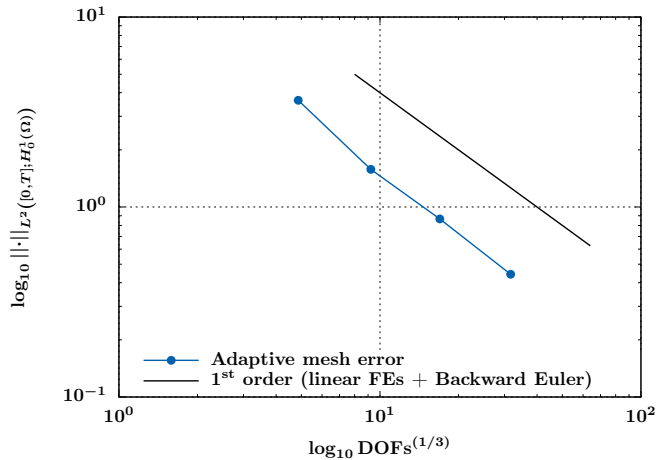


FIGURE 11. 3D semi-analytical benchmark problem. Convergence test.

**6.2. Strong-scaling analysis.** Next, the focus is turned to analysing the performance of FEMPAR-AM with a strong-scaling analysis<sup>2</sup>. The model problem for the subsequent experiments is designed to be geometrically simple, but with a computational load comparable to a real scenario of an industrial application.

According to this, the object of simulation is now the printing of 48 layers of 31.25 [μm] on top of a 32x32x16 [mm] prism. After printing the 48 layers, the prism has dimensions of 32x32x17.5 [mm], as shown in Fig. 12(a).

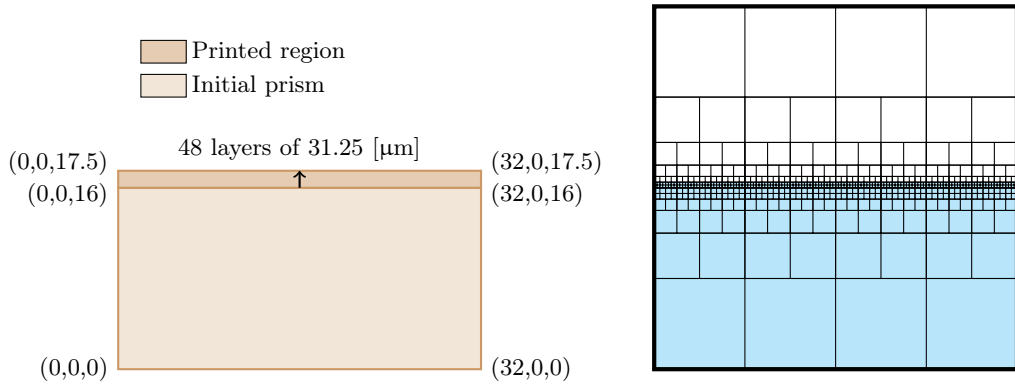
Concerning the process parameters, the power of the laser is set to 400 [W], the volumetric deposition rate during scanning is  $d_p = 10.0$  [mm<sup>3</sup>/s] and the time allowed for lowering the platform, recoating and layer relocation between layers is  $t_r = 10.0$  [s].

<sup>2</sup>Strong scalability is the ability of a parallel system (i.e. algorithm, software and parallel computer) to efficiently exploit increasing computational resources (CPU cores, memory, etc.) in the solution of a fixed-size problem. An *ideally* strongly scalable code decreases CPU time exactly as  $1/P$ , where  $P$  is the number of processors being used. In other words, if the system solves a size  $N$  problem in time  $t$  with a single processor, then it is able to solve the same problem in time  $t/P$  with  $P$  processors.

Apart from that, the material chosen is the Ti6Al4V Titanium alloy. The temperature dependent density, specific heat and thermal conductivity are obtained from a handbook and plotted in [25].

A constant heat convection boundary condition applies on the boundary of the cube with  $h_{\text{out}} = 50$  [W/m<sup>2</sup>K] and  $u_{\text{out}} = 35$  [°C]. The initial temperature of both the prism and each new layer is  $u_0 = 90$  [°C].

The root octree mesh is defined to cover a 32x32x32 [mm] cube region. The octree is transformed during the simulation to model the layer-by-layer deposition process, by prescribing a maximum refinement level of 11, i.e. assigning a mesh size of  $h = 32,000/2^{11} = 15.625$  [μm], to the elements inside the layer that is currently being printed. A mesh gradation is then established according to the distribution of thermal gradients (highest at the printing region, lowest at the bottom of the cuboid). The mesh size in the  $(x, y)$  plane is fixed, whereas it decreases in both  $z$ -directions, until reaching a minimum level of refinement of 4 at the top and bottom of the prism. The computational domain is then defined by the initial prism and the layers that have been printed up to the current time. As seen in Fig. 12(b), most elements end up concentrating around the current layer, due to the aggressive coarsening induced by the 2:1 balance, but this is also the region with the highest temperature variations.



(A) Setting of the example. The initial prism and the printed region are plotted in light and dark brown.  
 (B) Illustration of the refinement strategy for maximum and minimum refinement levels of 8 and 3, resp. Computational domain in light cyan.

FIGURE 12. Strong scaling analysis problem set up. Plane XZ view of the setting and the mesh.

This refinement strategy leads to a simulation workflow that, for each layer, comprises the following steps:

- (1) **Remeshing:** The previous mesh is refined and coarsened to accommodate the current layer.
- (2) **Redistribution:** The new mesh is partitioned and redistributed among all processors to maintain load balance.
- (3) **Activation:** New DOFs are distributed and initialized over the cells within the current layer.
- (4) **Printing:** The problem is solved for the printing step. This step consists in the application of the heat needed to fuse the powder of the current layer (step (2) of Fig. 6) and the time increment is calculated as  $\Delta t = t_p = V_{\text{layer}}/d_p$  [s].
- (5) **Cooling:** The problem is solved for the cooling step, accounting for lowering of building platform, recoat time and laser relocation (steps (3) and (1) of Fig. 6) with a time increment of  $\Delta t = t_r$  [s]. During the cooling step, the laser is off and the prism is allowed to cool down.

According to this workflow, the simulation of each layer is carried out in two time steps, printing and cooling, so the total number of time steps is  $48 \cdot 2 = 96$ . However, with the exception of the first layer, each new layer is meshed with a single refine and coarsen step. Hence, the simulation has about half

as many AMR events as time steps. Besides, the linear system in Eq. (12), arising at each time step, is solved with the BDDC(f)-Preconditioned Conjugate Gradient (PCG) method.

The numerical experiments for this example were run at the Marenostrum-IV [55] (MN-IV) supercomputer, hosted by the Barcelona Supercomputing Center (BSC). It is equipped with 3,456 compute nodes connected together with the Intel OPA HPC network. Each node has 2x Intel Xeon Platinum 8160 multi-core CPUs, with 24 cores each (i.e. 48 cores per node) and 96 GBytes of RAM.

Apart from that, FEMPAR-AM was compiled with Intel Fortran 18.0.1 using system recommended optimization flags and linked against the Intel MPI Library (v2018.1.163) for message-passing and the BLAS/LAPACK and PARDISO available on the Intel MKL library for optimized dense linear algebra kernels and sparse direct solvers, respectively. All floating-point operations were performed in IEEE double precision.

The parallel algorithm is set up such that each subdomain is associated to a different MPI task, with a one-to-one mapping among MPI tasks and CPU cores. In the BDDC framework, these are referred to as the *fine* tasks. Following the two-level algorithm in [8], the *coarse* duties are carried out by an additional MPI task, which is mapped to a full node, i.e. it has access to all its memory (96 GBytes) and computational resources (48 cores). The multithreaded sparse direct solvers in PARDISO are then employed for the solution of the coarse problem, by mapping as many threads to cores available in the node.

An effort was done in order to tune, with performance and scalability in mind, the values of the relevant parameters affecting the behaviour of the two-level BDDC(f) customized for growing domains. The resulting algorithm-parameter values combination is referred to as BDDC-ref. In particular, regarding dynamic load balancing, the partition weights are set to  $w_a = 10$  for active cells and  $w_i = 1$  for inactive cells. As for the coarse subgraph extraction procedure of Sect. 4.2, the maximum allowed degree  $\Delta^{\max}$  is 20, while the maximum allowed distance  $d^{\max}$  is 3.

Likewise, the example was designed such that it filled, as much as possible, the available memory per node for the smallest number of subdomains considered in the analysis (2 nodes, 96 cores / fine tasks). Following this criterion and using linear FEs, the average total number of cells  $N_{\text{cells}}$  and global DOFs  $N_{\text{dofs}}$  (excluding hanging DOFs) across all time steps are 12,585,216 and 10,273,920. Note that, if a fixed uniform mesh was used, specifying the maximum refinement level of 11 all over the cube, the number of cells would be  $(2^{11})^3 = 8.59 \cdot 10^9$  and the number of DOFs would grow from  $(2^{11}+1)^2(2^{11}/2+1) = 4.30 \cdot 10^9$ , initially, to  $(2^{11}+1)^3 = 8.60 \cdot 10^9$ , at the end of the simulation. Hence, it is readily exposed how  $h$ -adaptivity drastically reduces (almost by three orders of magnitude) the size of the problem and the required computational resources, while preserving accuracy around the growing printing region.

Fig. 13 and Tab. 1 compare the speed-up and the total simulation wall time [s] of BDDC-ref against a non-preconditioned parallel implementation of the Conjugate Gradient (CG) method, as the number of subdomains is increased. As observed, BDDC-ref scales up to 3,072 fine tasks with a peak speed-up of 8.8. Above 3,072 cores, time-to-solution increases due to parallelism related overheads; more computationally intensive simulations (i.e. larger loads per processor) would be required to exploit additional computational resources efficiently. However, CG saturates about six times earlier at 576 processors because interprocessor communication dominates the time devoted to solve the linear system. Moreover, CG is about 35% slower than BDDC-ref. With PCG-BDDC the total wall time reduces with the number of subdomains to approximately 6 minutes, whereas CG is not able to simulate the 48 layers in less than 20 minutes. The superiority of PCG-BDDC with respect to CG will even be stronger as larger total problem sizes are considered (i.e.  $h \rightarrow 0$ ), due to the fact that only PCG-BDDC is weakly scalable<sup>3</sup>.

---

<sup>3</sup>Weak scalability is the ability of a parallel system to efficiently exploit increasing computational resources in the solution of a problem *with fixed local size per processor*. An *ideally* weakly scalable code does not vary the time-to-solution with the number of processors and fixed local size per processor. In other words, if the system solves a problem in time  $t$  with a given amount of processors, then it is able to solve also in time  $t$  an  $X$  times larger problem with  $X$  times the number of processors.

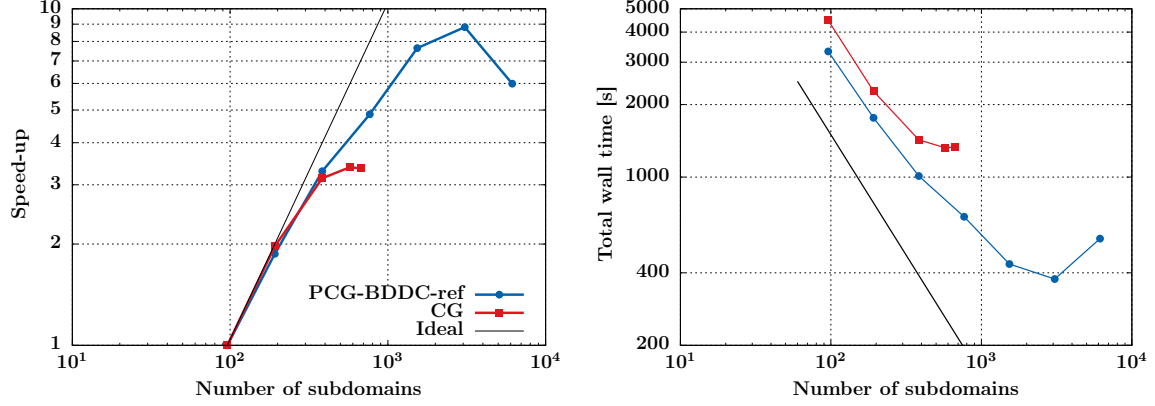


FIGURE 13. Strong scaling analysis: Results of BDDC-ref vs CG. BDDC-ref takes  $(w_a, w_i) = (10, 1)$ ,  $\deg^{\max} = 20$  and  $d^{\max} = 3$ . Compared to CG, BDDC-ref achieves higher scalability and faster runtimes.

		Total wall time [s]		$S_P = \frac{t_{96}}{t_P}$		$E_P = \frac{S_P}{P/96}$		$\bar{n}_{\text{dofs}}^{\text{local}}$	$\bar{n}_{\text{dofs}}^{\text{coarse}}$	$\bar{n}^{\text{iters}}$
P	BDDC	CG	BDDC	CG	BDDC	CG	Both	BDDC	BDDC	CG
96	3,325	4,475	1.00	1.00	1.00	1.00	111,812	354	27	3828
192	1,762	2,273	1.87	1.97	0.94	0.98	56,390	755	31	3822
384	1,010	1,427	3.29	3.14	0.82	0.78	28,533	1,582	39	3824
576	-	1,323	-	3.38	-	0.56	19,197	-	-	3823
672	-	1,334	-	3.35	-	0.48	17,737	-	-	3821
768	684	-	4.86	-	0.61	-	14,508	3,328	49	-
1,536	435	-	7.64	-	0.48	-	7,418	7,004	63	-
<b>3,072</b>	<b>377</b>	-	<b>8.82</b>	-	<b>0.28</b>	-	<b>3,827</b>	<b>14,750</b>	<b>78</b>	-
6,144	555	-	5.99	-	0.09	-	1,993	29,828	93	-

TABLE 1. Strong scaling analysis results of BDDC-ref vs CG. BDDC-ref takes  $(w_a, w_i) = (10, 1)$ ,  $\Delta^{\max} = 20$  and  $d^{\max} = 3$ . Total wall time accounts for the computational time of all simulation stages.  $S_P$  is the speed-up,  $E_P$  is the parallel efficiency,  $\bar{n}_{\text{dofs}}^{\text{local}}$  is the average size of the local fine problem (size of  $K^i$ ) across processors and time steps,  $\bar{n}_{\text{dofs}}^{\text{coarse}}$  is the average size of the coarse problem (size of  $A_C$ ) and  $\bar{n}^{\text{iters}}$  is the average number of iterations of the CG solver, both among time steps. At  $P = 3,072$  maximum speed up with BDDC is achieved.

Another point of interest is to analyse the fraction of total wall time of BDDC-ref dedicated to different phases of the simulation and their scalability. As observed in Fig. 14, almost two thirds of the computational time is devoted to the setup of the BDDC and the solution of the linear system at each printing and cooling step. This is partly related to the fact that there are twice as many linear system solutions as AMR steps. This evidence reinforces the convenience of selecting partition weights

in the search of equal distribution of DOFs among processors, and thus higher parallel efficiency in this stage (see Sect. 3.2). In addition, the speed-up of the total simulation is also governed by the solver. Even if the triangulation phase is the least scalable, the solver phase is the one determining when BDDC-ref loses parallel efficiency. In fact, this is a typical behaviour of two-level preconditioners: Although average iteration counts increase mildly with the number of processors, the size of the coarse problem keeps growing, while the local problems become smaller. Therefore, at some point, the coarse solver, which only exploits a bounded number of cores (i.e. those in a single compute node in this experiment), dominates computing times, loosing parallel efficiency. Fortunately, there is a large room for improvement in this direction, e.g. a multilevel version of the preconditioner is expected to push forward the limits of the presented strong scalability results (see, e.g. [9]).

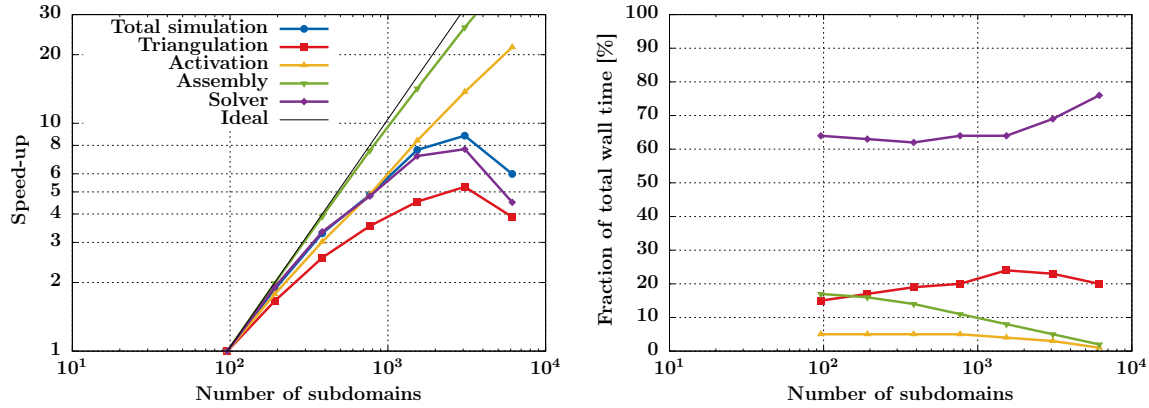


FIGURE 14. Strong scaling analysis: Results of BDDC-ref per simulation phases. The *triangulation* phase accounts for the remesh and redistribute steps of the simulation workflow, including projections and redistributions of the FE solution, whenever the mesh is transformed or redistributed. The *activation* phase accounts for the generation of the FE space with new DOFs assigned within the current layer. The *assembly* phase consists of local integration of the weak form and construction of the global linear system, during printing and cooling steps. Finally, the *solver* phase includes the setup of the BDDC and the solution of the linear system, also during printing and cooling steps. Although the triangulation phase is the least scalable, computational time and scalability in this example are dominated by the solver phase.

Further insights are drawn by studying the local distribution of cells and DOFs in space (among processors) and in time (among layers) up to 3,072 processors. As the number of cells and DOFs vary for each layer, all geometrical quantities are studied in terms of the mean  $\mu$  and the coefficient of variation  $c_v$ , also known as relative standard deviation, which is the ratio of the standard deviation  $\sigma$  to the mean  $\mu$ .  $c_v$  measures the extent of variability in relation to  $\mu$ . Thus, it can be used to compare the variability among different quantities.

Given a quantity  $x(t, p)$  that depends on the time step and processor, the time average at every processor is represented as  $\mu^t(x)$ , the average among processors at every time step as  $\mu^p(x)$  and the mean value across processors and time steps as  $\mu(x)$ . For quantities that only depend on time or processors, the superscripts are omitted.

In what follows, the magnitude of  $x$  is studied with  $\mu(x)$ , whereas two measures are chosen to study the dispersion:

- (1) The coefficient of variation among processors, i.e.  $c_v^p(x) = \mu^p(x)/\sigma^p(x)$ , when  $x = x(t, p)$  depends on both time step and processor. This statistic informs about possible computational load unbalances, due to an uneven distribution of  $x$  among processors. As  $c_v^p(x)$  depends on

the time step, for the sake of simplicity, the average across time steps  $\mu(c_v^p(x))$  is reported instead.

(2) The coefficient of variation among time steps  $c_v$ , when  $x = x(t)$  only depends on the time step.

Tab. 2 gathers the local distribution of cells and degrees of freedom (excluding the hanging ones). The values of  $\mu(c_v^p(x))$  show that the local number of cells is slightly unbalanced, but the local weighted number of cells, i.e. the sum of the cell weights at each processor for  $(w_a, w_i) = (10, 1)$ , is perfectly balanced. Apart from that, Fig. 15 shows that the number of cells oscillates with the height of the layer, but it does not grow in time. This behaviour propagates to other quantities such as the number of active cells or DOFs and it is caused by the aggressive 2:1 balance: The cells concentrate at the current layer and immediately below. Even if the domain grows in time, the number of cells away from the layer is much smaller than the number of those close or at the layer.

P	n <sub>cells</sub>		n <sub>weighted</sub> cells		n <sub>active</sub> cells		n <sub>dofs</sub>		n <sub>interface</sub> dofs	
	$\mu$	$\mu(c_v^p)$	$\mu$	$\mu(c_v^p)$	$\mu$	$\mu(c_v^p)$	$\mu$	$\mu(c_v^p)$	$\mu$	$\mu(c_v^p)$
96	131.0k	0.75	1114k	0.00	109.2k	0.10	111.8k	0.37	4.8k	34.4
192	65.5k	1.02	557k	0.01	54.6k	0.14	56.4k	0.45	3.3k	28.3
384	32.8k	1.44	279k	0.01	27.3k	0.20	28.5k	0.63	2.3k	25.8
768	16.4k	2.28	139k	0.02	13.7k	0.31	14.5k	0.73	1.6k	20.5
1,536	8.2k	3.46	69.6k	0.05	6.8k	0.48	7.4k	1.10	1.1k	20.7
3,072	4.1k	5.46	35.8k	0.09	3.4k	0.76	3.8k	1.39	0.8k	16.6

TABLE 2. Strong scaling analysis. Case PCG-BDDC-ref. Local distribution of cells and degrees of freedom (excluding hanging).  $\mu(c_v^p)$  expressed in %.

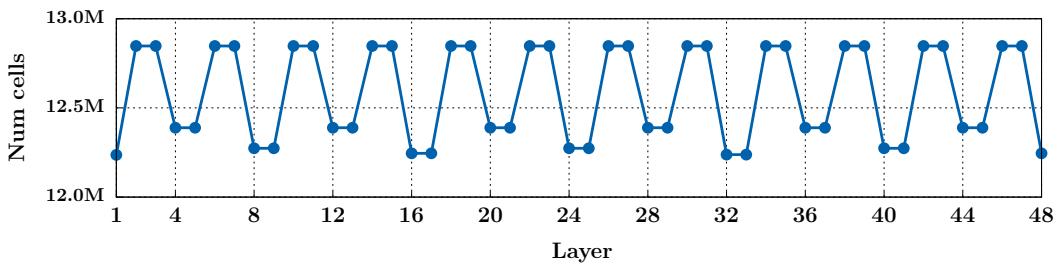


FIGURE 15. Evolution of global number of cells with the height of the layer.

It is also apparent that the pair  $(w_a, w_i) = (10, 1)$  effectively equilibrates the number of active cells among processors. Hence, the degrees of freedom are also evenly distributed, though with a slightly higher dispersion. This is especially beneficial for the integration and assembly phases, as they are implemented in FEMPAR, such that the bulk of the computational load is concentrated on the active cells set, and also the linear solver phase, as the size of the local systems depend on the number of DOFs that the processor owns. On the other hand, the mesh generation, refinement, coarsening and redistribution phases suffer from an uneven distribution of total cells. However, as discussed in Sect. 3.2 and assessed here in Fig. 14, these tend to be secondary phases in terms of computational time.

Concerning the local number of interface DOFs in Tab. 2, high variations in space expose the frequent irregularity of the Z-curve partitions. Even if the partition becomes increasingly regular with

$P$ , the imbalance of interface DOFs must be a source of MPI wait time in important operations of the non-preconditioned CG such as the matrix-vector product. As for BDDC, the negative effects of this imbalance are possibly relevant in the constrained Neumann solver for large  $P$ , when the number of interior DOFs and interface DOFs are of the same order.

Table 3 informs about the number of neighbours (i.e. remote subdomains sharing at least one vertex), coarse DOFs, PCG iterations and coarse problem size. The average number of neighbours is always lower than the value for structured partitions (26 in 3D), but it is subject to a very high variability in space. In particular, especially at low  $P$ , there exist subdomains that are in contact with the remaining  $P - 1$  neighbours, i.e. cone coarse graphs. Despite this extreme variability, there is a more moderate variability in the number of coarse DOFs. Apart from that, although the mean value of coarse DOFs is slightly higher than the one for BDDC(f) with structured partitions (6 in 3D), the maximum value of local coarse DOFs grows with  $P$  at a smoother rate than the number of neighbours. These are benefits from using BDDC(f), combined with the coarse subgraph extraction algorithm. Still, a subdomain can concentrate more than a hundred coarse DOFs during the simulation, leading to severe imbalance and extra cost during the computation of the coarse basis.

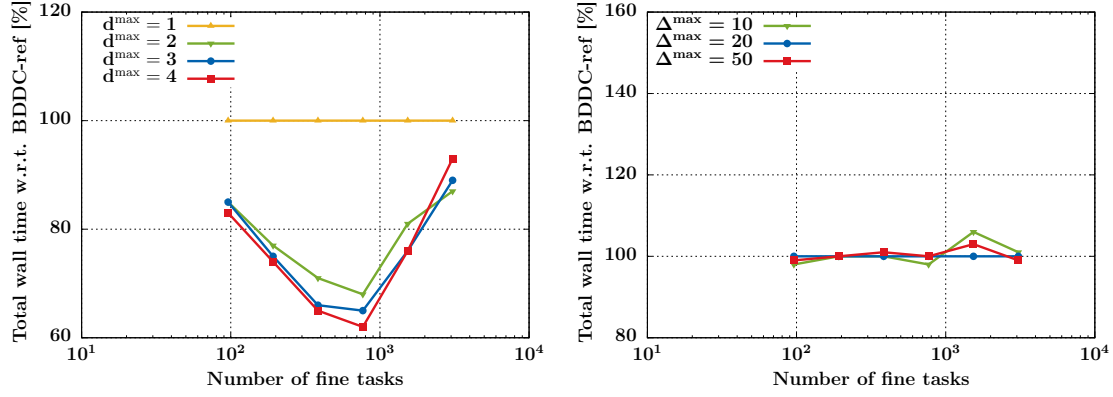
$P$	n <sub>neighbours</sub>			n <sub>coarse dofs</sub>			n <sub>PCG iters</sub>		n <sub>coarse dofs</sub> <sup>global</sup>	
	$\mu$	$\mu(c_v^p)$	max	$\mu$	$\mu(c_v^p)$	max	$\mu$	$c_v$	$\mu$	$c_v$
96	16	62.5	95	7	23.8	34	27	10.3	359	8.3
192	17	79.4	191	8	27.7	38	31	11.1	767	10.3
384	18	91.1	383	8	30.3	61	39	15.5	1,607	11.5
768	19	103.6	767	9	33.7	102	49	20.8	3,381	9.0
1,536	20	92.0	1,024	9	33.0	112	63	26.9	7,118	10.5
3,072	21	80.1	1,048	10	32.8	71	78	30.5	14,993	10.8

TABLE 3. Strong scaling analysis. Case PCG-BDDC-ref. Local distribution of neighbours and coarse degrees of freedom. Distribution of PCG iterations and coarse problem size.  $\mu(c_v^p)$  and  $c_v$  expressed in %.

In spite of this, removing redundant coarse DOFs clearly increases the efficiency and scalability of the framework, as shown in Fig. 16(a) with CPU time reductions ranging from 7 to 38 %. Furthermore, the maximum number of local coarse DOFs can be significantly reduced by increasing  $d^{\max}$  (see Fig. 17(a)). For instance, at  $P = 768$ , the maximum number of local coarse DOFs a processor assigned throughout the simulation drops more than tenfold from 870 at  $d^{\max} = 1$  (i.e. no subgraph extraction) to 64 at  $d^{\max} = 4$ . Further reductions could be achieved with higher  $d^{\max}$ , but this would not necessarily lead to better scaling results, because the cost of the extraction algorithm also becomes higher and it eventually turns into a bottleneck at the coarse task.

Conversely, the framework is not very sensitive to the maximum allowed degree  $\Delta^{\max}$  (see Fig. 16(b)). In practice, low values of  $\Delta^{\max}$  should be prescribed to optimize the BDDC method. However, this decision also diminishes the weight of this constraint with respect to the one for the maximum distance, to such a degree that the small variability shown in Fig. 16(b) cannot be discriminated from machine-related uncertainty.

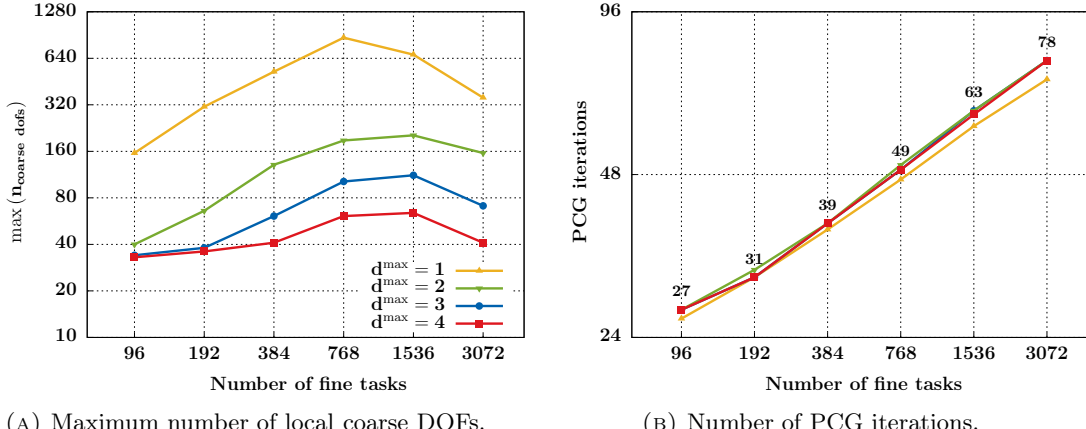
Returning to Tab. 3, the number of iterations grows with  $P$  at a moderate rate. Likewise, there is a large variability of the number of iterations from one time step to the other. As for the extraction algorithm, the number of PCG iterations is hardly affected by the reduction of coarse DOFs, even after increasing  $d^{\max}$  up to four, as seen in Fig. 17(b). In other words, the BDDC(f) method remains well-posed and practically optimal at low values of  $d^{\max}$ , as expected from the discussion in Sect. 4.



(a) Sensitivity to maximum allowed distance  $d^{\max}$ . Fraction of total wall time with respect to BDDC-ref without coarse subgraph extraction (i.e.  $d^{\max} = 1$ ).

(b) Sensitivity to maximum allowed degree  $\Delta^{\max}$ . Fraction of total wall time with respect to BDDC-ref (i.e.  $\Delta^{\max} = 20$ ).

FIGURE 16. Strong scaling plots assessing the sensitivity of BDDC-ref with respect to the parameters of the coarse subgraph extraction algorithm.  $d^{\max} = 1$  refers to the case where the coarse graph remains untouched. Higher efficiency and scalability can be achieved removing redundant coarse DOFs, but the extraction algorithm eventually becomes a bottleneck at the coarse task. On the other hand,  $\Delta^{\max}$  does not vary significantly the results, as long as it is low enough.



(a) Maximum number of local coarse DOFs.

(b) Number of PCG iterations.

FIGURE 17. Sensitivity of BDDC-ref with respect to the maximum allowed distance  $d^{\max}$  of the coarse subgraph.  $d^{\max} = 1$  refers to the case where the coarse graph remains untouched. Increasing  $d^{\max}$  reduces the maximum number of local coarse DOFs, while barely affecting the performance of the solver. The number of PCG iterations over the points is referred to BDDC-ref.

Finally, motivated by the fact that the local problem size is fairly stable across time steps, as  $c_v(\mu^p(n_{\text{dofs}}^i)) \leq 6.2\%$  for any  $P$ , the performance of BDDC-ref for thermal AM is confronted against a steady 3D Poisson's problem with (1) similar local number of DOFs, (2) a uniformly structured mesh, (3) a uniform partition and (4) BDDC(f) as preconditioner. This standard problem is the optimal scenario for BDDC in terms of scalability and the comparison serves to assess the loss of performance caused by dealing with an  $h$ -adaptive growing domain.

The results of this comparison are shown in Fig. 18(a). For the standard Poisson's problem, the speed-up is superlinear, as most of the runtime is devoted at the solver phase (e.g. 87 % at 96 processors for BDDC setup + CG algorithm)<sup>4</sup>. In AM BDDC-ref, on the other hand, the imbalance of DOFs and coarse DOFs (also, to a lesser extent, the remesh and redistribute phases) are responsible for bringing down the scalability to sublinear rates. However, in both problems, the two-level BDDC saturates at the same number of processors. In this respect, Fig. 18(b) is clarifying, as it reveals that the coarse problem in AM BDDC-ref is only 1.5 times larger than in the Poisson's problem, but they grow at the same rate (almost linear). The use of a multilevel BDDC method will be required to maintain scalability at larger scales [9], together with a parallel version for the extraction algorithm used to eliminate redundant coarse DOFs.

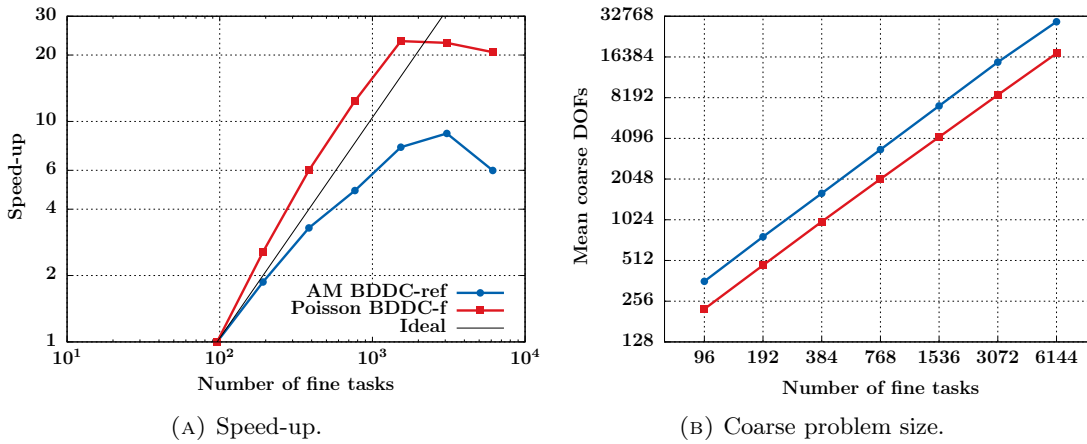


FIGURE 18. Strong scalability of AM BDDC-ref against a standard steady 3D Poisson's problem of the same local size. As expected, a significant amount of potential scalability is lost to deal with the growth of the domain. However, in both simulations, the coarse problem becomes a bottleneck at the same number of processors.

## 7. CONCLUSIONS

This work has introduced a novel HPC numerical framework for growing geometries that has been applied to the thermal FE analysis of metal additive manufacturing by powder-bed fusion at the part scale. The abstract framework is constructed from three main blocks (1) hierarchical AMR with octree meshes, distributed across processors with space-filling curves, (2) the extension of the element-birth method to a parallel environment, to track the growth of the geometry, and (3) a customization of BDDC, a highly scalable two-level preconditioner founded on DD methods, for the parallel linear solver.

After implementation in FEMPAR, an advanced object-oriented FE code for large scale computational science and engineering, a strong-scaling analysis considered the printing of 48 layers in a problem with 10 million unknowns. It exposed the two main bottlenecks for efficiency and scalability: the load imbalance of (1) DOFs, as the computational domain is a subset of the partitioned octree mesh, and (2) coarse DOFs, due to the irregularity of the mesh partition.

A weighted partition can effectively deal with (1); the weight function has been defined to seek a compromise between equally distributing among processors the number of cells or DOFs. As for (2), a coarse subgraph extraction algorithm has been proposed to identify and eliminate redundant coarse

<sup>4</sup>Sparse direct solvers are employed for the solution of local and coarse problems arising from the BDDC method. Given a linear system  $Ax = b$  of dimension  $N$ , it is well-known that the number of operations to compute  $x$  is  $\mathcal{O}(N^2)$ . If the solver phase is dominating, a superlinear speed-up should be observed.

DOFs. This procedure does not only equilibrates the coarse DOF distribution, it also reduces considerably the linear solver time, without disturbing the robustness and optimality of the preconditioner. After all these enhancements, the total wall time of the simulation was brought down to 377 [s] for 3,072 processors, i.e. the simulation of each layer (printing + cooling) lasted in average 8 [s].

Even if the adaptively growing nature of the problem hinders significantly the possibility to recover optimal scalability, in the sense of an ideal setting on a structured mesh and partition, it clearly compensates to adapt a high-end preconditioner, as it results in faster runtimes and higher scalability. In the case of BDDC, further scaling could be achieved through a multilevel extension [9]. On the other hand, the heuristic for reduction of coarse DOFs could also be of interest for other problems with highly-localized features treated with AMR and extended to a distributed multilevel version.

The numerical experiments with FEMPAR-AM have shown how this HPC framework could open the path to efficiently address levels of complexity and accuracy unseen in the literature of metal AM. Apart from turning to other part-scale physics in metal or polymer AM, it can also be exploited for other growing-geometry problems, as long as the growth is modelled by adding new elements to the computational mesh. Finally, with regards to possible industrial applications in AM, another interesting line of work is to blend the framework with unfitted FE methods [6, 14] to eliminate the mesh generation step for complex AM geometries and permit a coarsening of the mesh without affecting much the geometrical error.

## 8. ACKNOWLEDGEMENTS

Financial support from the EC - International Cooperation in Aeronautics with China (Horizon 2020) under the *EMUSIC* project (*Efficient Manufacturing for Aerospace Components USing Additive Manufacturing, Net Shape HIP and Investment Casting*), the EC - Factories of the Future (FoF) Programme under the *CA×Man* Project (*Computer Aided Technologies for Additive Manufacturing*) within *Horizon 2020* Framework Programme and the Spanish Government-MINECO-Proyectos de I+D (Excelencia)-DPI2017-85998-P-ADaMANT-Computational Framework for Additive Manufacturing of Titanium Alloy are gratefully acknowledged. The authors thankfully acknowledge the computer resources at Marenostrum-IV and the technical support provided by the Barcelona Supercomputing Center (RES-ActivityID: FI-2018-2-0009). E. Neiva gratefully acknowledges the support received from the Catalan Government through a FI fellowship. S. Badia gratefully acknowledges the support received from the Catalan Government through the ICREA Acadèmia Research Program. Financial support to CIMNE via the CERCA Programme / Generalitat de Catalunya is also acknowledged.

## REFERENCES

- [1] M. Ainsworth and J. T. Oden. *A posteriori error estimation in finite element analysis*, volume 37. John Wiley & Sons, 2011.
- [2] A. Anca, V. D. Fachinotti, G. Escobar-Palafox, and A. Cardona. Computational modelling of shaped metal deposition. *International Journal for Numerical Methods in Engineering*, 85(1): 84–106, 2011.
- [3] B. Awerbuch, M. Luby, A. V. Goldberg, and S. A. Plotkin. Network decomposition and locality in distributed computation. In *Foundations of Computer Science, 1989, 30th Annual Symposium on*, pages 364–369. IEEE, 1989.
- [4] S. Badia and H. Nguyen. Balancing domain decomposition by constraints and perturbation. *SIAM Journal on Numerical Analysis*, 54(6):3436–3464, 2016. ISSN 0036-1429, 1095-7170. doi: 10.1137/15M1045648.
- [5] S. Badia and M. Olm. Space-time balancing domain decomposition. *SIAM Journal on Scientific Computing*, 39(2):C194–C213, 2017.
- [6] S. Badia and F. Verdugo. Robust and scalable domain decomposition solvers for unfitted finite element methods. *Journal of Computational and Applied Mathematics*, 2017.

- [7] S. Badia, A. F. Martín, and J. Principe. Implementation and scalability analysis of balancing domain decomposition methods. *Archives of Computational Methods in Engineering*, 20(3):239–262, 2013.
- [8] S. Badia, A. F. Martín, and J. Principe. A highly scalable parallel implementation of balancing domain decomposition by constraints. *SIAM Journal on Scientific Computing*, 36(2):C190–C218, 2014.
- [9] S. Badia, A. F. Martin, and J. Principe. Multilevel balancing domain decomposition at extreme scales. *SIAM Journal on Scientific Computing*, 38(1):C22–C52, 2016.
- [10] S. Badia, A. F. Martín, E. Neiva, and F. Verdugo. On a highly parallel octree-based h-adaptive generic finite element simulation pipeline. *Submitted*, 2018.
- [11] S. Badia, A. F. Martín, and H. Nguyen. Physics-based balancing domain decomposition by constraints for multi-material problems. 2018.
- [12] S. Badia, A. F. Martín, and J. Principe. FEMPAR: An object-oriented parallel finite element framework. *Arch. Comput. Methods Eng.*, 25(2):195–271, 2018.
- [13] S. Badia, A. F. Martín, and J. Principe. FEMPAR Web page. <http://www.fempar.org>, 2018.
- [14] S. Badia, F. Verdugo, and A. F. Martín. The aggregated unfitted finite element method for elliptic problems. *Computer Methods in Applied Mechanics and Engineering*, 336:533–553, 2018.
- [15] W. Bangerth, C. Burstedde, T. Heister, and M. Kronbichler. Algorithms and data structures for massively parallel generic adaptive finite element codes. *ACM Transactions on Mathematical Software (TOMS)*, 38(2):14, 2011.
- [16] S. Brenner and R. Scott. *The mathematical theory of finite element methods*, volume 15. Springer Science & Business Media, 2007.
- [17] G. Bugeda, M. Cervera, and G. Lombera. Numerical prediction of temperature and density distributions in selective laser sintering processes. *Rapid Prototyping Journal*, 5(1):21–26, 1999.
- [18] C. Burstedde, L. C. Wilcox, and O. Ghattas. p4est: Scalable algorithms for parallel adaptive mesh refinement on forests of octrees. *SIAM Journal on Scientific Computing*, 33(3):1103–1133, 2011. doi: 10.1137/100791634.
- [19] C. Burstedde, J. Holke, and T. Isaac. Bounds on the number of discontinuities of morton-type space-filling curves. *arXiv preprint arXiv:1505.05055*, 2015.
- [20] H. Carslaw and J. Jaeger. *Conduction of heat in solids*. Oxford Science Publications: Oxford, UK, 1959.
- [21] M. Cervera, C. Agelet De Saracibar, and M. Chiumenti. Thermo-mechanical analysis of industrial solidification processes. *International Journal for Numerical Methods in Engineering*, 46(9):1575–1591, 1999.
- [22] M. Chiumenti, C. A. de Saracibar, and M. Cervera. On the numerical modeling of the thermo-mechanical contact for metal casting analysis. *Journal of Heat Transfer*, 130(6):061301, 2008.
- [23] M. Chiumenti, M. Cervera, N. Dialami, B. Wu, L. Jinwei, and C. Agelet de Saracibar. Numerical modeling of the electron beam welding and its experimental validation. *Finite Elements in Analysis and Design*, 121:118–133, 2016.
- [24] M. Chiumenti, X. Lin, M. Cervera, W. Lei, Y. Zheng, and W. Huang. Numerical simulation and experimental calibration of additive manufacturing by blown powder technology. part i: thermal analysis. *Rapid Prototyping Journal*, 23(2):448–463, 2017.
- [25] M. Chiumenti, E. Neiva, E. Salsi, M. Cervera, S. Badia, J. Moya, Z. Chen, C. Lee, and C. Davies. Numerical modelling and experimental validation in selective laser melting. *Additive Manufacturing*, 18(Supplement C):171 – 185, 2017. ISSN 2214-8604. doi: <https://doi.org/10.1016/j.addma.2017.09.002>.
- [26] K. D. Cole, J. V. Beck, A. Haji-Sheikh, and B. Litkouhi. *Heat conduction using Green's functions*. CRC Press, 2010.
- [27] C. A. De Saracibar, M. Cervera, and M. Chiumenti. On the formulation of coupled thermoplastic problems with phase-change. *International journal of plasticity*, 15(1):1–34, 1999.
- [28] E. R. Denlinger, V. Jagdale, G. V. Srinivasan, T. El-Wardany, and P. Michaleris. Thermal modeling of Inconel 718 processed with powder bed fusion and experimental validation using in

situ measurements. *Additive Manufacturing*, 11:7–15, 2016. ISSN 2214-8604.

- [29] E. R. Denlinger, M. Gouge, J. Irwin, and P. Michaleris. Thermomechanical model development and in situ experimental validation of the Laser Powder-Bed Fusion process. *Additive Manufacturing*, 16:73–80, 2017.
- [30] A. J. Dunbar, E. R. Denlinger, M. F. Gouge, and P. Michaleris. Experimental validation of finite element modeling for laser powder bed fusion deformation. *Additive Manufacturing*, 12, Part A: 108–120, 2016.
- [31] A. Ern and J.-L. Guermond. *Theory and practice of finite elements*, volume 159. Springer Science & Business Media, 2013.
- [32] V. D. Fachinotti, A. A. Anca, and A. Cardona. Analytical solutions of the thermal field induced by moving double-ellipsoidal and double-elliptical heat sources in a semi-infinite body. *International Journal for Numerical Methods in Biomedical Engineering*, 27(4):595–607, 2011.
- [33] J. Goldak, A. Chakravarti, and M. Bibby. A new finite element model for welding heat sources. *Metallurgical transactions B*, 15(2):299–305, 1984.
- [34] H. Haverkort and F. van Walderveen. Locality and bounding-box quality of two-dimensional space-filling curves. In *European Symposium on Algorithms*, pages 515–527. Springer, 2008.
- [35] N. E. Hodge, R. M. Ferencz, and R. M. Vignes. Experimental comparison of residual stresses for a thermomechanical model for the simulation of selective laser melting. *Additive Manufacturing*, 12, Part B:159–168, 2016.
- [36] J. Irwin and P. Michaleris. A Line Heat Input Model for Additive Manufacturing. *Journal of Manufacturing Science and Engineering*, 138(11):111004–111004–9, 2016.
- [37] T. Isaac, C. Burstedde, L. C. Wilcox, and O. Ghattas. Recursive algorithms for distributed forests of octrees. *SIAM Journal on Scientific Computing*, 37(5):C497–C531, 2015.
- [38] G. Karypis and V. Kumar. A Fast and High Quality Multilevel Scheme for Partitioning Irregular Graphs. *SIAM Journal on Scientific Computing*, 20(1):359–392, 1998. doi: 10.1137/S1064827595287997.
- [39] G. Karypis and V. Kumar. Parallel Multilevel series k-Way Partitioning Scheme for Irregular Graphs. *SIAM Review*, 41(2):278–300, 1999. ISSN 0036-1445. doi: 10.1137/S0036144598334138.
- [40] L. Kaufman and H. Bernstein. *Computer calculation of phase diagrams with special reference to refractory metals*. Academic Press New York, 1970. ISBN 012402050.
- [41] T. Keller, G. Lindwall, S. Ghosh, L. Ma, B. M. Lane, F. Zhang, U. R. Kattner, E. A. Lass, J. C. Heigel, Y. Idell, et al. Application of finite element, phase-field, and calphad-based methods to additive manufacturing of ni-based superalloys. *Acta materialia*, 139:244–253, 2017.
- [42] A. Kergaßner, J. Mergheim, and P. Steinmann. Modeling of additively manufactured materials using gradient-enhanced crystal plasticity. *Computers & Mathematics with Applications*, 2018.
- [43] S. A. Khairallah, A. T. Anderson, A. Rubenchik, and W. E. King. Laser powder-bed fusion additive manufacturing: Physics of complex melt flow and formation mechanisms of pores, spatter, and denudation zones. *Acta Materialia*, 108:36–45, 2016.
- [44] A. Klawonn and O. B. Widlund. Dual-primal feti methods for linear elasticity. *Communications on Pure and Applied Mathematics: A Journal Issued by the Courant Institute of Mathematical Sciences*, 59(11):1523–1572, 2006.
- [45] A. Klawonn, O. B. Widlund, and M. Dryja. Dual-primal feti methods for three-dimensional elliptic problems with heterogeneous coefficients. *SIAM Journal on Numerical Analysis*, 40(1):159–179, 2002.
- [46] S. Kollmannsberger, A. Özcan, M. Carraturo, N. Zander, and E. Rank. A hierarchical computational model for moving thermal loads and phase changes with applications to selective laser melting. *Computers and Mathematics with Applications*, 75(5):1483 – 1497, 2018. ISSN 0898-1221. doi: <https://doi.org/10.1016/j.camwa.2017.11.014>.
- [47] S. Kolossov, E. Boillat, R. Glardon, P. Fischer, and M. Locher. 3d FE simulation for temperature evolution in the selective laser sintering process. *International Journal of Machine Tools and Manufacture*, 44(2–3):117–123, 2004.

- [48] P. Küs and J. Šítek. Coupling parallel adaptive mesh refinement with a nonoverlapping domain decomposition solver. *Advances in Engineering Software*, 110:34–54, 2017.
- [49] Y. Lian, S. Lin, W. Yan, W. K. Liu, and G. J. Wagner. A parallelized three-dimensional cellular automaton model for grain growth during additive manufacturing. *Computational Mechanics*, 61(5):543–558, 2018. doi: 10.1007/s00466-017-1535-8.
- [50] L.-E. Lindgren. *Computational welding mechanics*. Elsevier, 2014.
- [51] L.-E. Lindgren, A. Lundbäck, M. Fisk, R. Pederson, and J. Andersson. Simulation of additive manufacturing using coupled constitutive and microstructure models. *Additive Manufacturing*, 12:144–158, 2016.
- [52] X. Lu, X. Lin, M. Chiumenti, M. Cervera, J. Li, L. Ma, L. Wei, Y. Hu, and W. Huang. Finite element analysis and experimental validation of the thermomechanical behavior in laser solid forming of ti-6al-4v. *Additive Manufacturing*, 21:30–40, 2018.
- [53] A. Lundbäck and L.-E. Lindgren. Modelling of metal deposition. *Finite Elements in Analysis and Design*, 47(10):1169–1177, 2011.
- [54] J. Mandel and C. R. Dohrmann. Convergence of a balancing domain decomposition by constraints and energy minimization. *Numerical linear algebra with applications*, 10(7):639–659, 2003.
- [55] Marenostrum-IV website. <https://www.bsc.es/marenostrum/marenostrum>, (n.d.). Accessed: 2018-07-24.
- [56] T. Mathew. *Domain decomposition methods for the numerical solution of partial differential equations*, volume 61. Springer Science & Business Media, 2008.
- [57] P. Michaleris. Modeling metal deposition in heat transfer analyses of additive manufacturing processes. *Finite Elements in Analysis and Design*, 86:51–60, 2014.
- [58] G. M. Morton. A computer oriented geodetic data base and a new technique in file sequencing. 1966.
- [59] L. Parry, I. Ashcroft, and R. Wildman. Understanding the effect of laser scan strategy on residual stress in selective laser melting through thermo-mechanical simulation. *Additive Manufacturing*, 12:1–15, 2016.
- [60] N. Patil, D. Pal, H. Khalid Rafi, K. Zeng, A. Moreland, A. Hicks, D. Beeler, and B. Stucker. A Generalized Feed Forward Dynamic Adaptive Mesh Refinement and Derefinement Finite Element Framework for Metal Laser Sintering—Part I: Formulation and Algorithm Development. *Journal of Manufacturing Science and Engineering*, 137(4):041001, 2015.
- [61] P. Prabhakar, W. Sames, R. Dehoff, and S. Babu. Computational modeling of residual stress formation during the electron beam melting process for Inconel 718. *Additive Manufacturing*, 7:83–91, 2015.
- [62] I. A. Roberts, C. J. Wang, R. Esterlein, M. Stanford, and D. J. Mynors. A three-dimensional finite element analysis of the temperature field during laser melting of metal powders in additive layer manufacturing. *International Journal of Machine Tools and Manufacture*, 49(12–13):916–923, 2009.
- [63] T. M. Rodgers, J. D. Madison, and V. Tikare. Simulation of metal additive manufacturing microstructures using kinetic Monte Carlo. *Computational Materials Science*, 135:78–89, 2017. doi: 10.1016/J.COMMATS.2017.03.053.
- [64] E. Salsi, M. Chiumenti, and M. Cervera. Modeling of microstructure evolution of ti6al4v for additive manufacturing. *Metals*, 8(8):633, 2018.
- [65] I. Setien, M. Chiumenti, S. van der Veen, M. San Sebastian, F. Garciandía, and A. Echeverría. Empirical methodology to determine inherent strains in additive manufacturing. *Computers & Mathematics with Applications*, 2018.
- [66] J. Šítek, M. Čertíková, P. Burda, and J. Novotný. Face-based selection of corners in 3d substructuring. *Mathematics and Computers in Simulation*, 82(10):1799–1811, 2012.
- [67] J. Smith, W. Xiong, J. Cao, and W. K. Liu. Thermodynamically consistent microstructure prediction of additively manufactured materials. *Computational mechanics*, 57(3):359–370, 2016.
- [68] J. C. Steuben, A. P. Iliopoulos, and J. G. Michopoulos. Towards Multiscale Topology Optimization for Additively Manufactured Components Using Implicit Slicing. In *Volume 1: 37th Computers*

and Information in Engineering Conference, page V001T02A024. ASME, 2017. doi: 10.1115/DETC2017-67596.

- [69] A. Toselli and O. Widlund. *Domain decomposition methods-algorithms and theory*, volume 34. Springer Science & Business Media, 2006.
- [70] T. Wohlers. *Wohlers report 2017*. Wohlers Associates, Inc, 2017.
- [71] W. Yan, S. Lin, O. L. Kafka, Y. Lian, C. Yu, Z. Liu, J. Yan, S. Wolff, H. Wu, E. Ndip-Agbor, M. Mozaffar, K. Ehmann, J. Cao, G. J. Wagner, and W. K. Liu. Data-driven multi-scale multi-physics models to derive process–structure–property relationships for additive manufacturing. *Computational Mechanics*, 61(5):521–541, May 2018. doi: 10.1007/s00466-018-1539-z.
- [72] W. Yan, Y. Qian, W. Ge, S. Lin, W. K. Liu, F. Lin, and G. J. Wagner. Meso-scale modeling of multiple-layer fabrication process in selective electron beam melting: Inter-layer/track voids formation. *Materials and Design*, 141:210 – 219, 2018. doi: <https://doi.org/10.1016/j.matdes.2017.12.031>.
- [73] Y. P. Yang, M. Jamshidinia, P. Boulware, and S. M. Kelly. Prediction of microstructure, residual stress, and deformation in laser powder bed fusion process. *Computational Mechanics*, 61(5):599–615, 2018. doi: 10.1007/s00466-017-1528-7.